

**Deep Mixing in Evolved Stars:  
I. The Effect of Reaction Rate Revisions from C to Al.**

S. Palmerini<sup>1</sup>, M. La Cognata<sup>2</sup>, S. Cristallo<sup>3</sup>, & M. Busso<sup>1</sup>

Received \_\_\_\_\_; accepted \_\_\_\_\_

---

<sup>1</sup>Dipartimento di Fisica, Università di Perugia, and INFN, Sezione di Perugia;  
sara.palmerini@fisica.unipg.it

<sup>2</sup>Dipartimento di Metodologie Fisiche e Chimiche per l'Ingegneria, Università di Catania,  
Catania, Italy and Laboratori Nazionali del Sud - INFN, Catania, Italy

<sup>3</sup>Departamento de Física Teórica y del Cosmos, Universidad de Granada, Spain

## ABSTRACT

We present computations of nucleosynthesis in low-mass red-giant-branch and asymptotic-giant-branch stars of Population I experiencing extended mixing. We adopt the updated version of the FRANEC evolutionary model, a new post-process code for non-convective mixing and the most recent revisions for solar abundances. In this framework, we discuss the effects of recent improvements in relevant reaction rates for proton captures on intermediate-mass nuclei (from carbon to aluminum). For each nucleus we briefly discuss the new choices and their motivations. The calculations are then performed on the basis of a parameterized circulation, where the effects of the new nuclear inputs are best compared to previous works. We find that the new rates (and notably the one for the  $^{14}\text{N}(p,\gamma)^{15}\text{O}$  reaction) imply considerable modifications in the composition of post-main sequence stars. In particular, the slight temperature changes due to the reduced efficiency of proton captures on  $^{14}\text{N}$  induce abundance variations at the first dredge up (especially for  $^{17}\text{O}$ , whose equilibrium ratio to  $^{16}\text{O}$  is very sensitive to the temperature). In this new scenario presolar oxide grains of AGB origin turn out to be produced almost exclusively by very-low mass stars ( $M \leq 1.5 - 1.7M_{\odot}$ ), never becoming C-rich. The whole population of grains with  $^{18}\text{O}/^{16}\text{O}$  below 0.0015 (the limit permitted by first dredge up) is now explained. Also, there is now no forbidden area for very low values of  $^{17}\text{O}/^{16}\text{O}$  (below 0.0005), contrary to previous findings. A rather shallow type of transport seems to be sufficient for the CNO changes in RGB stages. Both thermohaline diffusion and magnetic-buoyancy-induced mixing might provide a suitable physical mechanism for this. Thermohaline mixing is in any case certainly inadequate to account for the production of  $^{26}\text{Al}$  on the AGB. Other transport mechanisms must therefore be at play. In general, observational constraints from RGB and

AGB stars, as well as from presolar grains, are well reproduced by our approach. An exception remains the nitrogen isotopic ratio in mainstream SiC grains. For the low values measured in them (i.e. for  $^{14}\text{N}/^{15}\text{N} \leq 2000$ ) we have no explanation. Actually, for the several grains with subsolar nitrogen isotopic ratios no known stellar process acting in low mass stars can provide a clue. This might be an evidence that some form of contamination from cosmic ray spallation occurs in the interstellar medium, adding fresh  $^{15}\text{N}$  to the grains.

## 1. Introduction

It is now well known that the processes of astration and gas return to the Interstellar Medium (ISM) of galaxies is dominated by low mass (LM) and intermediate mass (IM) stars, i.e. by objects below  $M = 7\text{-}8 M_{\odot}$  (Sedlmayr 1994). These stars share the properties of ascending, after the Main Sequence, along the Red Giant Branch (RGB) and then, after the occurrence of core-He burning, of terminating their evolution through the so-called Asymptotic Giant Branch (AGB) stage (see e.g. Iben & Renzini 1983). Here they lose mass efficiently thanks to radial pulsations and to radiation pressure on dust grains (Herwig 2005; Guandalini et al. 2006; Guandalini & Busso 2008), powering stellar winds that are enriched with the products of the internal nucleosynthesis. Tiny solid particles that are abundant in such winds maintain the signature of those nuclear processes; samples of the most refractory among those grains can be recovered from pristine meteorites (Zinner 2005) and this fact has enormously increased the importance of AGB stars as laboratories for the study of H- and He-burning nucleosynthesis (Busso et al. 1999).

At the end of the AGB stage, the residual envelopes of LM and IM stars are lost through the fast ejection of hot, ionized materials (“superwind”); the circumstellar envelope, heated and illuminated by the now hot central star, forms a planetary nebula, while the

dense, electron-degenerate core starts a blue-ward path, which will ultimately give birth to a white dwarf (Van Winckel 2003; Prada Moroni et al. 2004). Stars crossing these evolutionary stages not only represent a fundamental component of the baryonic mass in galaxies, but also provide us with invaluable information on the physical and chemical evolution of the universe. As a consequence, the understanding of moderately massive stars is a necessary condition for addressing a large part of modern astrophysical problems.

Unfortunately, embarrassing gaps exist in our knowledge of their physics, and fundamental problems affecting their evolution are not properly treated in common stellar modeling. This is not surprising, as stellar models provide only a basic description, where important physical mechanisms (like convection) are oversimplified and others (e.g. rotation) are often neglected (see e.g. Charbonnel & Lagarde 2010, for a recent outline of the importance of rotation). One big problem affecting low-mass-star evolutionary models is revealed by the isotopic ratios of CNO elements, as observed in stellar photospheres (Harris et al. 1985; Cottrell & Sneden 1986; Gilroy & Brown 1991; Shetrone et al. 1993; Smiljanic et al. 2009) and in presolar grains of AGB origin, preserved in meteorites (see Nittler et al. 1997; Choi et al. 1998; Amari et al. 2001).

Some chemical peculiarities concerning light elements are found very early in stellar evolution (Richard et al. 2005; Meléndez et al. 2009). Others appear slightly after the occurrence of the first dredge up (hereafter FDU), where stars populate the so-called *bump* of the luminosity function (Charbonnel 2004). Then the appearance of anomalies in the composition continues along the AGB phase (Wasserburg et al. 1994; Busso et al. 2010). The observational basis for these issues has grown considerably over the years, confirming chemical anomalies at least from Li to O, but sometimes extending up to Mg and Al, including the production of the unstable isotope  $^{26}\text{Al}$  (see e.g. Pilachowsky et al. 1993; Charbonnel 1994; Gratton et al. 2000; Grundahl et al. 2002; Busso et al. 2003; Zinner et al.

2006; Nittler et al. 2008).

The above evidence suggests that non-convective transport mechanisms occur in stars, especially during the RGB and AGB phases, linking the envelope to regions where proton captures occur (Sweigart & Mengel 1979; Boothroyd et al. 1994; Charbonnel 1995; Charbonnel & Do Nascimento 1998; Nollett et al. 2003)

Secular mixing phenomena are made easy in RGB and AGB phases immediately following an episode of convective dredge-up, because the H-burning shell then advances in homogeneous regions, so that the natural barrier opposed to mass transport by the chemical stratification is not present. Mechanisms of this kind might actually account for several puzzling astrophysical observations: from the evolution of  $^3\text{He}$  in the ISM (Wasserburg et al. 1994; Glöcker & Geiss 1998; Bania et al. 2002) to the complex phenomena of production and destruction of Li in the Galaxy, including its long-term decline in main sequence stars (Spiegel 1972; Spiegel and Zahn 1992; Zahn 1994) and its re-production in some (rare) red giants (Charbonnel & Balachandran 2000; Guandalini et al. 2009). Further implications of slow mixing probably include the anti-correlations displayed by globular cluster stars, involving intermediate mass elements up to Mg and appearing already on the Main Sequence (Gratton et al. 2001; Thévenin et al 2001; Ramirez & Cohen 2002). Indeed, they might have been inherited from LM or IM progenitors, hosting proton captures in mixing episodes through the AGB phases.

Among the processes involved in deep-mixing phenomena, those induced by rotation certainly play an important role (Zahn 1992; Charbonnel & Lagarde 2010), despite difficulties in explaining the observed isotopic ratios (Palacios et al. 2006). Actually, a shear layer, at the contact between the differentially rotating convective envelope and the more rigid stellar core is a natural expectation (see e.g. Kippenhahn & Weigert 1990). A rigid-body behavior in the cores of low-mass stars might be linked to an interplay of

magnetic coupling and meridional circulation (Eggenberger et al. 2005).

Despite formal differences in the various approaches, most models considered the chemical mixing induced by rotational effects (and the associated angular momentum transport) as a diffusive process, with parameterized diffusion coefficients (see e.g. Denissenkov et al. 1998; Denissenkov & Weiss 1996, 2000; Weiss et al. 2000). This approach has also been adopted in modeling massive, stratified stars, e.g. by Maeder & Meynet (2004). Alternatives were presented by Denissenkov & Tout (2003), who studied the effects of gravitational waves, and by Busso et al. (2007a); Nordhaus et al. (2008); Denissenkov et al. (2009). These last authors discussed the effects of magnetic buoyancy induced by a stellar dynamo. The presence of such a dynamo in red giants finds supports in some stellar variability observations (Andrews et al. 1988) and in the identification of surface magnetic fields in AGB stars (Herpin et al. 2006). Stellar magnetic fields and their instabilities have been also the object of previous detailed analysis (Spruit 1999, 2002). However, by far the most popular scenario in recent years has been that of the so-called *thermohaline* diffusion, induced by an inversion in the molecular weight  $\mu$ . In H-burning regions this is due to the activation of the reaction  ${}^3\text{He}+{}^3\text{He} \rightarrow {}^4\text{He} + 2\text{p}$  (Eggleton et al. 2006, 2008; Charbonnel & Zahn 2007), which locally reduces  $\mu$ . The phenomenon is more general than that; it was recognized long time ago and it can occur in other astrophysical contexts (Stothers & Simon 1969; Ulrich 1972).

Diffusive mechanisms (such as thermohaline mixing) and circulation phenomena (like those induced e.g. by magnetic buoyancy) yield abundance changes that are sometimes undistinguishable from one another, sometimes remarkably different, depending on the velocity of the transport. Verifying whether observations can provide clues to discriminate among the possible physical processes generating the mixing is therefore an important issue. In this respect, interesting new elements have been offered by the recent 2D- and

3D-calculations by Denissenkov (2010); Denissenkov & Merryfield (2010). After presenting our results, we shall comment in some detail on these elements, especially in comparison with what magnetic buoyancy can a priori provide.

Before the effects of different, uncertain mixing models can be addressed, however, one has preliminarily to ascertain that the normalizing solar abundances and the nuclear input data be very reliable. Using all the upgrades appeared in the recent literature on these issues, we intend to revisit the coupled processes of proton capture nucleosynthesis and of deep mixing in red giants, starting from a parameterized analysis (where nuclear and abundance effects are best compared to previous work). In section 2 we shall present a general discussion of the set of new inputs adopted, postponing to a dedicated Appendix the details of the reaction rate choices made. In section 3 we shall then discuss recent upgrades and novelties in stellar models and in section 4 we shall briefly illustrate our technique for performing parameterized, post-process deep-mixing calculations, starting from the results of the FRANEC evolutionary code. Then in sections 5 and 6 we shall outline the nucleosynthesis results thus obtained, showing some comparisons with previous work, with stellar observations and with presolar grain measurements of isotopic abundances for elements from C to Al. Comments on recent models for thermohaline mixing in 2 and 3 dimensions are then added in a dedicated section (section 7). Finally, some general conclusions are drawn in section 8.

## **2. On Recent Revisions in Solar Abundances and Reaction Rates**

A previous parameterized analysis of extra-mixing in red giants (Nollett et al. 2003) adopted solar abundances from Anders & Grevesse (1989), coupled with the general prescriptions for reaction rates from the compilation by Angulo et al. (1999), hereinafter simply referred to as NACRE. Since then, however, many remarkable changes have occurred

in both sets of input data. For what concerns solar abundances, we shall in general adopt the compilation by Asplund et al. (2009), implying a total solar metallicity of  $Z = 0.014$ . We underline that not only elemental, but also isotopic abundances (as updated in that review) are important for our analysis; this is especially the case for CNO elements. In particular, we shall make use of the new estimate of the  $^{15}\text{N}/^{14}\text{N}$  ratio, as deduced by studies of the Jovian atmosphere (Fouchet et al. 2000; Owen et al. 2001); for it we adopt the value derived by the Composite Infrared Spectrometer onboard the Cassini spacecraft ( $2.22 \pm 0.52 \times 10^{-3}$ , a factor 1.5 smaller than the terrestrial one), which should represent the initial solar-system ratio (Fouchet et al. 2004). For oxygen isotopes we use the values suggested by Asplund et al. (2009).

Concerning reaction rates, recent extensive reviews have been published, summarizing the main experimental changes occurred after the NACRE compilation, which has been the reference in most papers on low-mass stellar nucleosynthesis over the last decade. In particular, we shall discuss here (and adopt throughout the paper) the recommendations by Adelberger et al. (2010) and Iliadis et al. (2010), hereinafter simply referred to as ADE10 and ILI10, respectively. We instead will not analyze the work by Beard et al. (2010), which pertains to stellar burning at much higher temperatures and to nucleosynthesis in high-density environments. The work by ADE10 represents the follow-up of the solar-fusion cross-section review by Adelberger et al. (1998) and includes subsequent measurements for reactions of the pp chain and of CNO cycles. It mainly focuses on low-energy cross sections, aiming at extracting the rates for temperatures typical of the solar core ( $T_9^1 \sim 0.015$ ). Reaction rates are obtained analytically, in terms of low-energy expansion coefficients of the astrophysical  $S(E)$  factors. The work by ILI10 is instead an upgrade of the previous review by Iliadis et al. (2001). In the new work several improvements have been introduced:

---

<sup>1</sup>For the temperature we adopt the notation where  $T_9 = T/10^9\text{K}$ .



(i) a wider range of atomic masses is covered, from  $A=14$  to  $A=40$ , including some CNO reactions; (ii) updated nuclear physics inputs are considered in the reaction rate evaluation; (iii) a calculation procedure improved with respect to that of Iliadis et al. (2001) is adopted. In detail, a suited probability distribution is first associated with each nuclear physics quantity entering the reaction-rate calculation. Then, the reaction rate itself is computed for a set of input parameter values, which are randomly taken, each following the appropriate distribution. In this way, a probability density function is generated for the reaction rate reflecting the distribution of the input values. This method has the important consequence that the upper and lower limits are estimated with a statistically-appropriate approach, so that a really meaningful value can be attributed to them. Moreover, the rate is obtained over a wide temperature range  $T_9 = 0.01 - 10$ , almost reaching down to the values found at the inner borders of the convective envelopes in low-mass AGB stars ( $T_9 \sim 0.005$ ). It is worth remarking that both compilations, ADE10 and ILI10, account for the recent results obtained using indirect techniques, such as the Coulomb Dissociation (Baur & Rebel 1994), the Asymptotic Normalization Coefficient (Mukhamedzhanov et al. 1997) and the Trojan Horse Method (La Cognata et al. 2010a). This makes the low-temperature reaction rates more accurate, thanks to the possibility of extending the measurements down to the astrophysical range of energies.

The recommended reaction rates from ADE10 and ILI10 differ, sometimes remarkably, from NACRE results. This fact (and the search for the descending astrophysical consequences) is the main motivation for the present work.

Proton capture reactions on nitrogen and oxygen isotopes are of special importance in our context. In particular, the reaction rate for  $^{14}\text{N}(p,\gamma)^{15}\text{O}$  by ADE10, reduced by 50% with respect to NACRE, leads to a reduction in the efficiency of the whole CNO cycling, moving the H-burning shell toward inner stellar regions, where temperature and

density values are higher by about 10% and 25%, respectively, as compared to previous stellar models. We shall discuss at length the important consequences of these facts on the envelope abundances. As we shall see, also the new data for proton captures on  $^{17}\text{O}$  induce non-negligible effects on the surface composition. By contrast, no appreciable effect derives from the reduction in the rate for  $^{15}\text{N}(p,\gamma)^{16}\text{O}$ ; in fact, it modifies the abundances of  $^{16}\text{O}$ ,  $^{17}\text{O}$ ,  $^{18}\text{O}$  and  $^{19}\text{F}$  only in the regions where the H-burning efficiency is maximum ( $T_9 > 0.05$ ), which are untouched by deep mixing.

In general, we use the ADE10 compilation for pp-chain and CNO-cycle reactions, while we adopt the results from ILI10 for heavier nuclei. However, the two compilations partly overlap in the region of CNO isotopes. In this case, specific choices are necessary. In order to motivate them, and to illustrate some of the novelties with respect to NACRE, we present in the Appendix a discussion of the available data for some key reactions and of our choice.

### 3. The new reference stellar models

Although we have certainly achieved a general understanding of the conditions under which chemical elements are produced in stellar interiors, a predictive nucleosynthesis theory based on first principles is still lacking. A basic missing ingredient in developing such a theory is a full understanding of the transport properties of the turbulent, reactive plasma in which the elements are forged. Within this context, many efforts have been spent in the past years to study the properties of the final phases of stellar evolution by means of theoretical models calculated with the Frascati RAphson-Newton Evolutionary Code (FRANEC: see Chieffi et al. 1998). As an example, the extra-mixing calculations by Nollett et al. (2003), which represent the starting point of the present work, were based on FRANEC stellar structures taken from Straniero et al. (2003). This last work

presented parameterized theoretical formulae permitting a simple derivation of the physical characteristics of AGB stars (such as, for example, the number of thermal pulses, the mass of the H-exhausted core and of the envelope, the stellar surface temperature and so on), by interpolating the outputs of previously-computed full AGB evolutionary models (Straniero et al. 1997).

Calculations presented in this paper are instead based on new evolutionary stellar sequences. In particular, we have performed complete runs (from the pre-Main Sequence to the end of the AGB phase) for a  $1.5 M_{\odot}$  star and a  $2.0 M_{\odot}$  star, with a metallicity equal to the most recent estimate for the solar one (Cristallo et al. 2009a). The runs have been performed with an upgraded version of the FRANEC code. Computations extending up to the RGB tip have also been included for various other masses in the range 1 -  $1.7 M_{\odot}$ . Our calculations do not yet include rotation, nor the effects of magnetic fields. However, as compared to older versions of the FRANEC stellar code (Straniero et al. 1997), the models here adopted represent a remarkable improvement, including several new or updated ingredients.

Among the main differences with respect to the previous scenario we recall: i) the use of a full nuclear network, coupled with the physical evolution; ii) the adoption of an updated solar chemical distribution (in particular, the code was revised in the last years using the Lodders 2003, compilation).<sup>2</sup> We remind that older versions of FRANEC used instead the abundances by Anders & Grevesse (1989), which are substantially different; iii) the use of new reaction rates, of which crucial is in particular the new value for the  $^{14}\text{N}(p,\gamma)^{15}\text{O}$  reaction (see the Appendix for details); in the FRANEC code this update was originally

---

<sup>2</sup>In the post process we use the updated suggestions by Asplund et al. (2009): the small differences between this set of data and the one used in the stellar code does not introduce any consequence on the model physics.

implemented when the measurements by the LUNA experiment became available (Imbriani et al. 2005; Lemut et al. 2006); iv) the adoption of new low-temperature opacities and their modifications during the evolution, when the envelope chemical admixture is changed by dredge up and becomes carbon rich (Cristallo et al. 2007); v) the choice, in evolved stages, of a mass loss law different from the one previously used; this relation is similar to the one by Vassiliadis & Wood (1993), but adopts more recent data on the Period-Luminosity relation of AGB stars (see Straniero et al. 2006, for details); vi) a different treatment of the radiative/convective interfaces. In particular, instead of using a bare Schwarzschild criterion, an exponentially-decreasing profile of the convective velocities was applied at the inner border of the convective envelope (Cristallo et al. 2009a).

In any case, for a discussion of the improvements outlined above as items from i) to vi) and of their motivations see especially Cristallo et al. (2009a). For the scopes of this work, we want primarily to underline that the adoption of a full nuclear network (although it increases the computational time by a factor 15 to 40, depending on the case considered) has proven to be crucial. Indeed, computing a set of full models, with the evolution of all the abundances coupled to the structural and thermodynamic evolution, provides bona-fide abundance templates, on which to verify the outcomes of any post-process calculation done for specific purposes. These post-process studies remain necessary whenever many parameterized cases have to be considered (as is required, e.g., in the present paper). However, now their results (in terms of predicted abundances) can be validated carefully on a smaller set of complete FRANEC calculations. The inclusion of the extended network into the code was primarily motivated by other reasons. In fact, the usual approach of stellar models, to consider only the limited set of reactions controlling the energy generation, becomes completely inadequate whenever the physical properties of a structure are strongly related to the chemical composition changes. This is, e.g., the case of the proton ingestion by the convective shell driven by the first fully developed thermal pulse, which is found to

occur in very metal-poor AGB stars and during the post-AGB phases at larger metallicities. (Cristallo et al. 2009b; Herwig et al. 2010). More generally, the code with the full network can now be used to compute the nucleosynthesis in the He-shell (including *s*-processing). In the context of the present work verifying the post-process calculations with a (limited) set of checks from real, full-network models was important for those isotopes whose abundances are strongly influenced by the TDU. Typical examples of this are nuclei like  $^{22}\text{Ne}$  (produced in the thermal pulses),  $^{23}\text{Na}$  (that derives from proton and neutron captures on these same  $^{22}\text{Ne}$  seeds) and  $^{26}\text{Al}$ . This last nuclide is produced in the innermost H-burning zones, hence sinks into the He-rich buffer and is subsequently largely destroyed by neutron-captures at high temperature ( $T \geq 3 \times 10^8 K$ ) during the thermal pulses. The surviving part is then dredged up again to the H-rich layers and can account for  $^{26}\text{Al}/^{27}\text{Al}$  ratios in the envelope of up to  $5 - 6 \times 10^{-3}$ , which are then enhanced by the extra production of  $^{26}\text{Al}$  in deep mixing episodes.

As we shall discuss in next section, the new models imply important changes in the surface isotopic composition already on the RGB, at the occurrence of the FDU. In the final evolutionary stages, then, the effects are even more substantial, especially for what concerns the chemical enrichment of the envelope along the AGB.

#### 4. Computations of Extended Mixing and Nucleosynthesis

Starting from the models described in section 3, and also for the sake of comparison with previous works, we have performed parametric calculations, using as free parameters the rate of mass transport ( $\dot{M}$ ) and the maximum temperature sampled by the circulating material ( $T_P$ ), as in Nollett et al. (2003). This last parameter is best expressed by the difference  $\Delta = \log T_H - \log T_P$ , where  $T_H$  is the temperature at which the energy from the H-burning shell is maximum. We shall use this definition of  $\Delta$  throughout this paper;

similarly, we shall often express  $\dot{M}$  in units of  $10^{-6} M_{\odot}/\text{yr}$  and we shall call this parameter  $\dot{M}_6$ . We present here results mainly for solar-metallicity models of 1.5 and 2.0  $M_{\odot}$ , although some extra models have been computed for comparisons with observational data. The post-process calculations have been run in a way similar to what was done previously, using older releases of the same FRANEC stellar code (Nollett et al. 2003; Busso et al. 2010). The post-process program is new and its results have been cross-checked with the ones obtained with the older code (Palmerini et al. 2008).

During RGB stages, we have introduced extra-mixing after the "bump" of the luminosity function (BLF), i.e. after the H-burning shell has erased the chemical discontinuity left behind by the FDU (Charbonnel 1996). We shall not repeat here a general discussion of RGB physics, as it can be easily found elsewhere (Charbonnel & Balachandran 2000; Palacios et al. 2006). Our procedure in the calculations was illustrated by Palmerini et al. (2009). We have followed the abundance changes during the transport due to nucleosynthesis (partial derivatives with respect to time) and to displacements across the integration grid (partial derivatives with respect to distance, times the mixing velocity). One can write this synthetically as:

$$\frac{dY_i}{dt} = \frac{\partial Y_i}{\partial t} + \dot{M} \cdot \frac{\partial Y_i}{\partial M}$$

Here  $Y_i$  is the abundance by mole of the  $i$ -th isotope (for the present work, this index spans from H to  $^{32}\text{S}$ ). In agreement with Nollett et al. (2003) and with Busso et al. (2010) the fractional areas  $f_u$  and  $f_d$  occupied by the upward and downward mass transport, respectively, have been set to be  $f_u = f_d (\equiv f) = 0.5$ . When this analysis is pursued in the framework of a slow mixing process, the physical mechanism of transport and its velocity do not play any crucial role; the nucleosynthesis results are then controlled by the path integral of reaction rates over the trajectory. If needed, the mixing velocity  $v$  can then be simply derived as:  $v = \frac{1}{f} \times \frac{\dot{M}}{4\pi r^2 \rho}$ . As discussed elsewhere (Guandalini et al. 2009),

very different scenarios may open up when the transport is operated by fast mechanisms, suitable to yield mixing time scales comparable to (or shorter than) the  ${}^7\text{Be}$  half-life. The complex processes associated to the nucleosynthesis of low mass nuclei like D,  ${}^3\text{He}$ , Li, Be and B will however be postponed to another work.

After core He-exhaustion, our low-mass stellar models evolve to the AGB stages. General discussions of the physics of AGB stars can be found in Iben & Renzini (1983); Busso et al. (1999); Straniero et al. (2006). On the AGB, deep mixing phenomena can occur again, and there is actually clear observational evidence of their presence in those final stages (Busso et al. 2010). In fact, below the convective envelopes of these evolved red giants, conditions of chemical homogeneity similar to those found after FDU are established. During the early phase of the AGB (before thermal pulses start) this is guaranteed by the previous advancement of the H-burning shell during the first ascent to the RGB. Subsequently, when thermal instabilities from the He shell begin, the downward envelope expansions (which follow them) easily reach down to the H-He discontinuity, even before the penetration into the He-rich layers occurs, a fact that formally defines the third dredge up, or TDU. In most of the interpulse periods of AGB phases, therefore, H burning proceeds in an initially-homogeneous environment, i.e. in conditions suitable for the occurrence of extra-mixing.

Various experimental constraints (and in particular the spread in the C, O and Al isotopic ratios shown by presolar grains) suggest that the details of the transport vary from star to star (Nollett et al. 2003). One has also to mention that not all the physical mechanisms suitable to drive chemical transport in first-ascent red giants are necessarily available also during the AGB stages. This was discussed by Busso et al. (2010), who showed that the operation of deep mixing on the RGB, by whatever cause, consumes  ${}^3\text{He}$ , so that the molecular weight inversion generated by its burning occurs in AGB phases

only if the amount of  $^3\text{He}$  remaining in the envelope is substantial (as is the case in the work by Charbonnel & Lagarde 2010). Otherwise, different physical mechanisms must be looked for. In Fig.1 we better illustrate this point reporting the variation of the molecular weight ( $\mu$ ) across the radiative region of a 1.5 and a 2.0  $M_{\odot}$  star with solar metallicity. While the  $\mu$  inversion on the RGB is appreciable in both the considered models, on the AGB it is preserved only if a sufficient supply of  $^3\text{He}$  remains. In particular, for the AGB, different lines refer to different abundances of  $^3\text{He}$  resulting from the previous RGB phase: no destruction, a consumption by factors of 3 or 10. It is evident that the stronger the previous  $^3\text{He}$  consumption is, the weaker is the  $\mu$  inversion.

## 5. Results for the RGB phases

Table 1 illustrates the main changes in the nitrogen and oxygen isotopic ratios induced by FDU, for the sample case of a 1.5  $M_{\odot}$  star. In order to allow for comparisons with previous results and to disentangle the reasons of the changes, the table is presented for the solar metallicity and for the typical cases  $Z = 0.01$  and  $Z = 0.02$ , often used in deep mixing discussions. As a comparison, the values previously adopted by Nollett et al. (2003), taken from Boothrotd & Sackmann (1999) for the same stellar mass are also shown.

Table 1

Nitrogen and Oxygen Isotopes at First Dredge Up.

(1.5  $M_{\odot}$  models with updated reaction rates)

Case	$^{15}\text{N}/^{14}\text{N}$	$^{17}\text{O}/^{16}\text{O}$	$^{18}\text{O}/^{16}\text{O}$
$Z = 0.01$	$6.17 \cdot 10^{-4}$	$1.44 \cdot 10^{-3}$	$1.57 \cdot 10^{-3}$
$Z = 0.014 (\odot)$	$6.27 \cdot 10^{-4}$	$1.21 \cdot 10^{-3}$	$1.59 \cdot 10^{-3}$
$Z = 0.02$	$6.65 \cdot 10^{-4}$	$9.99 \cdot 10^{-4}$	$1.62 \cdot 10^{-3}$
Nollett et al. (2003)	$1.81 \cdot 10^{-3}$	$8.10 \cdot 10^{-4}$	$1.62 \cdot 10^{-3}$



Table 2  
 Nitrogen and Oxygen Isotopes at FDU  
 (Variation with reaction rates,  $Z = Z_{\odot}$ )

a): updating only the $^{14}\text{N}(p,\gamma)^{15}\text{O}$			
Mass ( $M_{\odot}$ )	$^{15}\text{N}/^{14}\text{N}$	$^{17}\text{O}/^{16}\text{O}$	$^{18}\text{O}/^{16}\text{O}$
1.0	$2.07 \cdot 10^{-3}$	$4.29 \cdot 10^{-4}$	$2.42 \cdot 10^{-3}$
1.2	$1.51 \cdot 10^{-3}$	$5.44 \cdot 10^{-4}$	$2.19 \cdot 10^{-3}$
1.5	$1.09 \cdot 10^{-3}$	$1.26 \cdot 10^{-3}$	$2.01 \cdot 10^{-3}$
1.7	$9.16 \cdot 10^{-4}$	$2.30 \cdot 10^{-3}$	$1.91 \cdot 10^{-3}$
2.0	$7.79 \cdot 10^{-4}$	$4.87 \cdot 10^{-3}$	$1.83 \cdot 10^{-3}$
b) ADE10 & ILI10 rates; new $[^{15}\text{N}/^{14}\text{N}]_{\odot}$			
Mass ( $M_{\odot}$ )	$^{15}\text{N}/^{14}\text{N}$	$^{17}\text{O}/^{16}\text{O}$	$^{18}\text{O}/^{16}\text{O}$
1.0	$1.19 \cdot 10^{-3}$	$3.81 \cdot 10^{-4}$	$1.89 \cdot 10^{-3}$
1.2	$8.64 \cdot 10^{-4}$	$4.82 \cdot 10^{-4}$	$1.73 \cdot 10^{-3}$
1.5	$6.27 \cdot 10^{-4}$	$1.11 \cdot 10^{-3}$	$1.58 \cdot 10^{-3}$
1.7	$5.25 \cdot 10^{-4}$	$2.04 \cdot 10^{-3}$	$1.51 \cdot 10^{-3}$
2.0	$4.46 \cdot 10^{-4}$	$4.32 \cdot 10^{-3}$	$1.44 \cdot 10^{-3}$

Table 1 reveals that the estimates for the surface isotopic ratios of nitrogen and oxygen at FDU can change by large amounts with respect to previous findings. In particular, this is true for  $^{15}\text{N}/^{14}\text{N}$  and for  $^{17}\text{O}/^{16}\text{O}$ . In order to show the selective relevance of the model choices in producing these results, Table 2 shows the same nitrogen and oxygen ratios as obtained: a) updating, with respect to Nollett et al. (2003), the physical model parameters, the value of the solar metallicity and the  $^{14}\text{N}(p,\gamma)^{15}\text{O}$  rate; and b) adding also all the other new reaction rates by ADE10 and ILI10, as discussed in section 2, and using the new (Jovian) value for the solar system nitrogen isotopic ratio. This is done for the masses 1, 1.2, 1.5, 1.7, 2  $M_{\odot}$ , at solar metallicity.

A comparison between the two tables makes clear that, while for nitrogen the change is mainly due to the choice of the new solar value, the large shifts for  $^{17}\text{O}/^{16}\text{O}$  descend from both the new abundances and the new rate for proton captures on  $^{14}\text{N}$ . Indeed, both the mentioned upgrades induce small but effective changes in the stellar structure, in particular in the temperature profile and in the maximum penetration of the envelope during the FDU. These changes are obviously larger for stars where CNO cycling is more efficient: our 2  $M_{\odot}$  model has  $^{17}\text{O}/^{16}\text{O} = 5.14 \times 10^{-3}$ , which is more than twice the value of  $2 \times 10^{-3}$ , previously used in deep mixing models by Nollett et al. (2003) and Boothrotd & Sackmann (1999). In this case, the new adopted solar metallicity increases the  $^{17}\text{O}/^{16}\text{O}$  by about 65%, while the new  $^{14}\text{N}(p,\gamma)^{15}\text{O}$  adds a further 35%. In the upper panel of Fig 2 we report the temperature profile at central hydrogen exhaustion characterizing four different 2  $M_{\odot}$  models, run with different inputs:

1. standard case (we shall call it ST); it has the new  $\sigma_{^{14}\text{N}}$  and  $Z = Z_{\odot}$ ;
2. test case with the new  $\sigma_{^{14}\text{N}}$  and  $Z=0.02$  (this is the solar metallicity derived by adopting the compilation of Anders & Grevesse 1989);
3. test case with the old  $\sigma_{^{14}\text{N}}$  and  $Z = Z_{\odot}$ ;

4. test case with the old  $\sigma_{14\text{N}}$  and  $Z=0.02$ .

The standard case shows the highest temperature profile, this fact leading to a larger  $^{17}\text{O}$  production in the region between 0.3 and 0.8  $M_{\odot}$  (the inner core is not affected by the FDU, while the external layers have temperatures too low to activate H-burning). In the lower panel of Fig.2 we report the abundances of hydrogen,  $^{16}\text{O}$  and  $^{17}\text{O}$  of our ST case. In the same panel we also report the maximum penetration of the convective envelope during FDU. Note that, although the envelope penetrates less than in the other tests ( $M_{\text{bottom}}^1=0.302$ ,  $M_{\text{bottom}}^2=0.290$ ,  $M_{\text{bottom}}^3=0.298$ ,  $M_{\text{bottom}}^4=0.286$ ), the standard case shows the largest  $^{17}\text{O}/^{16}\text{O}$  value, because of the strong dependence of this ratio on the temperature (see also Nollett et al. 2003, their Fig. 8 in particular).

A look at Table 2 reveals that the other reaction rate changes of section 2, including those directly affecting oxygen isotopes, induce smaller (although non-negligible) effects than the  $^{14}\text{N}(p,\gamma)^{15}\text{O}$  does, in altering the isotopic mix of oxygen at FDU.

Fig. 3 shows this in graphic form: filled squares represent the isotopic composition of oxygen at FDU in our models, while open squares show the previous situation, with the old NACRE rates and the old choice for the solar metallicity. The new results confine the stellar masses that produced presolar oxide grains within a very narrow range ( $1 \leq M/M_{\odot} \leq 1.5 - 1.7$ ).

The abundances seen at the surface of a giant star near the tip of the RGB are then known to differ from those at FDU for the effects of deep mixing phenomena, which change the envelope composition by linking its material to the hotter, radiative regions above the H-burning shell, where proton captures re-establish a varying abundance distribution, starting from an initially-homogeneous composition. Fig. 3 also shows the effects of deep mixing on the RGB (for a specific choice of the parameters defined in Section 4, namely  $\Delta = 0.15$  and  $\dot{M}_6 = 0.3$ ). As the figure shows, presolar grains with a moderate  $^{18}\text{O}$  destruction,

mainly of group 1 (Nittler et al. 1997), can be reproduced by this rather extreme processing, provided the stellar masses are confined within the range mentioned above. This range is the same where most MS-S stars are found. We shall come back on this point in the next section. Most grain data, however, and especially those with both  $^{18}\text{O}/^{16}\text{O}$  and  $^{17}\text{O}/^{16}\text{O}$  ratios below 0.0012, require even more extended processing than presented in the figure and clearly indicate that deep mixing cannot occur only on the RGB (see Busso et al. 2010).

Typical abundance profiles created by nucleosynthesis in the region below the convective envelope after the luminosity bump are shown in the four panels of Fig. 4 taken from our 2  $M_{\odot}$  model with initially solar composition. In regions below  $\Delta \simeq 0.2$  (corresponding to the vertical dashed line) the  $^3\text{He}+^4\text{He}$  reaction starts to dominate over the  $^3\text{He}+^3\text{He}$  one (that induces the inversion of the molecular weight); this is therefore the innermost position from which thermohaline diffusion can start. Notice that some remarkable abundance changes, including the production of a critical nucleus like  $^{23}\text{Na}$ , and an enhanced destruction of  $^{18}\text{O}$ , occur immediately below this zone. If only thermohaline mixing were to take care of transporting matter to the envelope on the RGB, then we would confirm the recent findings by Charbonnel & Lagarde (2010), according to which these nuclei are only moderately affected in RGB stages. If instead deeper mixing mechanisms were at play, this result would change drastically (as we have shown for the destruction of  $^{18}\text{O}$  in Fig. 3).

Indication on the mixing depth can obviously be derived by observational data. We must however recall that spectroscopic measurements, especially for isotopes, have very large uncertainties, so that their constraints should be used with care. Furthermore, the metallicity of Population I red giants spans over a large range, while our models cover only a factor-of-two interval. As a consequence, among the several existing compilations of CNO abundances for red giants of the galactic disk we can consider only those with metallicities in the range  $0.01 \leq Z \leq 0.02$ , as the interplay of nucleosynthesis and mixing is extremely

sensitive to metallicity variations. The best comparisons for our solar-metallicity cases ( $Z = 0.014$ ) should come from M67, whose composition has always been confirmed to be very close to solar (Randich et al. 2006). For this cluster CN abundances and  $^{12}\text{C}/^{13}\text{C}$  ratios were determined by Brown (1987) and Gilroy & Brown (1991), but the oxygen abundance was not measured and rather assumed from older works. New determinations of the oxygen concentration in M67 now exist (Tautvaišienė et al. 2000; Yong et al. 2005; Pancino et al. 2010) and their  $[\text{O}/\text{Fe}]$  ratios essentially agree with one another; however, other rather different suggestions are also available (Friel et al. 2010). We shall adopt here the  $[\text{O}/\text{Fe}]$  and  $[\text{Fe}/\text{H}]$  values by Yong et al. (2005), rescaling oxygen for our updated choice of the solar abundance from Asplund et al. (2009). The results of our  $Z = 0.02$  case can instead be compared to observations in evolved RGB stars of open clusters younger than the Sun, like e.g. those studied by Smiljanic et al. (2009) and Mikolaitis et al. (2010). Only few stars from samples of the old disk (see e.g. Cottrell & Sneden 1986; Shetrone et al. 1993) can instead be used for our purposes, namely those whose metallicity is close to solar. Fig. 5 shows a comparison of our models with observations selected according to the above criteria. Given the uncertainty of spectroscopic measurements (especially the older ones), the agreement is quite good, especially for M67. The observations do require deep mixing at a moderate temperature ( $\Delta = 0.2$ ) and at circulation rates  $0.1 \leq \dot{M}_6 \leq 0.3$ . From the value of  $\Delta$  we infer that thermohaline diffusion might be adequate for this purpose. However, warnings on the mixing velocity and on the diffusion coefficient deduced from recent literature have to be considered and we refer to section 7 for a more detailed discussion of that.

## 6. Results for the AGB phases

For the late evolutionary stages, the adoption of low temperature C-enhanced opacity tables, the choice of a new mass loss law (limiting the number of thermal pulses) and the different treatment of the inner convective border all play important roles in controlling the final results. While, again, we direct the reader to Cristallo et al. (2009a) for details, we need to recall here that the present AGB models have now a much stronger support from observations. In particular, the new opacities and the more effective mass loss law adopted combine in inducing lower values for the surface temperature and luminosity. In their turn, these facts affect the colors, the infrared emission and the luminosity function of AGB stars. The new models now succeed in reproducing the photometric and spectroscopic properties of their observational counterparts; in particular, the low effective temperatures of C stars at different metallicities (Domínguez et al. 2004; Busso et al. 2007b) can now be naturally reproduced. The stronger mass loss rates reduce the number of thermal pulses, but the introduction of an exponentially decaying profile of convective velocities at the base of the envelope increases the TDU efficiency, so that the final enhancement factor of the most significant nuclei produced by AGB stars is roughly the same as before; but now this is obtained together with a good reproduction of the luminosity functions of AGB stars (Cristallo et al. 2011, in preparation).

We also recall that the adopted algorithm for the velocity profile accounts, after each TDU episode, for the formation of a tiny region enriched in protons where, subsequently,  $^{13}\text{C}$  can be formed. This is the radiative  $^{13}\text{C}$  pocket where  $(\alpha, n)$  captures on  $^{13}\text{C}$  provide the main neutron source for the synthesis of heavy n-rich nuclei in AGB stars (see e.g. Busso et al. 1999; Lugaro et al. 2003; Straniero et al. 2006; Sneden et al. 2008), thus complementing the production of lighter n-rich nuclei in massive stars (see e.g. Busso & Gallino 1985; Raiteri et al. 1993; Käppeler et al. 1994; Pignatari et al. 2010). We however postpone the

analysis of this important point to a future paper.

Deep mixing in thermally-pulsing AGB stages operates on the composition established above the H-burning shell and homogenized after each pulse by the penetration of the convective envelope. Typical abundances established in those layers by proton captures are shown in Fig. 6. Previous work (Nollett et al. 2003; Busso et al. 2010) leads us to expect that extra mixing mainly operates down to regions where  $\Delta = 0.1$  to  $0.2$ . These zones can be identified in Fig. 6 from the two vertical lines. As is clear from the plots, remarkable nucleosynthesis changes are induced there by the adoption of the new reaction rates (continuous curves). Among the differences, we find a larger destruction of  ${}^3\text{He}$ ,  ${}^{15}\text{N}$ ,  ${}^{18}\text{O}$ ,  ${}^{19}\text{F}$  and a lower production of  ${}^{23}\text{Na}$ . This last result is directly linked to a lower destruction of  ${}^{21}\text{Ne}$  and  ${}^{22}\text{Ne}$ . The important radioactive nucleus  ${}^{26}\text{Al}$  is more effectively produced than before, but only marginally. In general, these results can be interpreted as due to the slight increase in the temperature induced by the new (less efficient) rate for  ${}^{14}\text{N}(p,\gamma){}^{15}\text{O}$ , superimposed to the specific effects of the rate changes for heavier nuclei, which have a more local and limited effect.

As a consequence of the model changes and of the reaction rate updates, the combined operation of mixing and nucleosynthesis leads now to abundance changes in the envelope like those summarized in Fig. 7 (for the  $1.5 M_{\odot}$  model) and in Fig. 8 (for the  $2 M_{\odot}$  model). For these examples we adopted, on the RGB,  $\Delta = 0.2$ ,  $\dot{M}_6 = 0.3$ ; on the AGB,  $\Delta = 0.1$ ,  $\dot{M}_6 = 1$ . These choices only serve for the purpose of illustration. A wider sample of cases for the AGB is presented in the subsequent Fig. 9 and Fig. 10<sup>3</sup>.

The above figures referring to the AGB clearly show a saw-tooth trend in the

---

<sup>3</sup>For researchers interested to comparisons with specific observations, looking for an even wider series of cases, we can provide the nucleosynthesis results upon request.

abundances of several nuclei. This is induced by the sudden mixing with He-rich layers at the third dredge up (TDU), after each pulse. This trend is therefore pronounced for those nuclei that are largely affected by He-shell nucleosynthesis, in particular  $^{12}\text{C}$ ,  $^{22}\text{Ne}$  and  $^{26}\text{Al}$ .

The  $^{12}\text{C}$ -enrichment by TDU is partly compensated by its destruction in deep-mixing processing during the inter-pulse stages. The operation of such mixing at even moderate efficiencies has the consequence of preventing the formation of a carbon star in our models up to  $1.7 M_{\odot}$ . Combining this with the changes already discussed for the FDU (see Fig. 3), we can say that both MS, S giants and oxide presolar grains should be produced mainly by stars below this mass limit. Obviously, a more massive star ( $2 M_{\odot}$  or more), before becoming C-rich, also passes through an O-rich phase in which TDU induces MS-S spectral characteristics; but the high efficiency of dredge-up we have now implies that this is a not a dominant phase. This can be inferred from the limited amount of mass lost in the O-rich stages by a  $2 M_{\odot}$  model star becoming C-rich. For moderate extra-mixing ( $\dot{M}_6 = 0.1$ ) this amounts to  $0.4$  and  $0.2 M_{\odot}$  at solar metallicity and at  $Z = 0.01$ , respectively. By contrast, more than  $1 M_{\odot}$  is lost in the C-rich phase. On the contrary, a  $1.5 - 1.7 M_{\odot}$  star loses its whole envelope (at least  $0.8 M_{\odot}$ ) in the form of O-rich material. If one also considers that the initial mass function favors these lower masses, one can deduce that most of the observed MS and S giants should have a mass smaller than for C-stars and that among these low mass AGB stars one should find the typical progenitors of presolar oxide grains. There is obviously a possibility of finding MS-S giants among intermediate mass stars ( $M \geq 4M_{\odot}$ ), where hot bottom burning prevents the formation of a carbon star. However, for them the expected isotopic ratios (especially for Oxygen) are very peculiar (e.g. with large excesses of  $^{17}\text{O}$ ). Iliadis et al. (2008), by comparisons of intermediate-mass models with presolar grain abundances, convincingly excluded any connection of IM stars with presolar grains; presently, we don't know of even one single grain really requiring an intermediate-mass progenitor.



We can see this in some more detail. As already stated in discussing the RGB phases and in Busso et al. (2010), oxygen isotopes in presolar oxide grains provide the most stringent constraints to stellar models with deep mixing, due to the fragility of  $^{18}\text{O}$  and to the sensitivity of  $^{17}\text{O}$  to temperature. Fig. 11 (left panel) presents these constraints, showing the oxygen isotopic ratios in group 1 and group 2 grains together with model curves. These last include typical trends for extra-mixing on the RGB at a moderate efficiency, plus the results of deep-mixing computations for the AGB, for various choices of the parameters. Notice that, by including the  $1 M_{\odot}$  star, the whole range of  $^{17}\text{O}/^{16}\text{O}$  ratios is covered. This is another effect of the model changes and corrects previous findings, based on older models, according to which the grains at the extreme left would not be explained by deep mixing at solar metallicity (Wasserburg et al. 1994; Nollett et al. 2003). The main reason of the change lays in the more marked destruction of  $^{18}\text{O}$  at moderate temperatures, where  $^{17}\text{O}$  is still untouched (see Fig. 4, second panel). This is found also in very low-mass models and allows their deep-mixing curves to proceed almost vertically, covering a previously unaccounted area (not only the new rate for the  $^{14}\text{N}(p,\gamma)^{15}\text{O}$ , but also those for proton captures on  $^{17}\text{O}$  are important in determining this result). The left panel of Fig. 11 also shows that the whole set of abundances for  $^{18}\text{O}$ -poor grains (with  $^{18}\text{O}/^{16}\text{O}$  ratios below 0.0015) is explained by models for stars below about  $1.7 M_{\odot}$ , those that will never become C rich.

The right panel of Fig. 11 then presents the  $^{17}\text{O}/^{16}\text{O}$  ratio as a function of  $^{26}\text{Al}/^{27}\text{Al}$ , for those grains that show  $^{26}\text{Mg}$  excesses from  $^{26}\text{Al}$  decay. Here  $\dot{M}_6$  is assumed to be 3 (a rather efficient case). Again, most of the experimental results can be accounted for. A small group of grains, for  $^{17}\text{O}/^{16}\text{O}$  ratios below 0.001 and  $^{26}\text{Al}/^{27}\text{Al}$  above 0.01, are however not explained. We notice here that no modification to the model might cover this area. In fact (as an example) mixing at higher temperature would improve the fit to  $^{26}\text{Al}$  but would worsen the problem for  $^{17}\text{O}$  (not to mention the fact that mixing at higher temperatures

would affect the stellar structure). There appears to be a unique way out: an increase in the reaction rate for the  $^{25}\text{Mg}(p,\gamma)^{26}\text{Al}$  reaction at temperatures sufficiently small to minimize the effects on  $^{17}\text{O}$ . In the energy region of our interest the main contribution to that reaction rate is due to resonances (at 58 and 93keV) for which large uncertainties are still present (Iliadis et al. 1996). We found that, by artificially increasing their strengths by a factor of 5 with respect to present recommendations, grains rich in  $^{26}\text{Al}$  and not in  $^{17}\text{O}$  can be accounted for (e.g. using  $\Delta = 0.05$  and  $\dot{M}_6 = 3$  in a  $1.2 M_\odot$  stellar model). We leave this suggestion for future verifications. Recent new measurements (especially from LUNA) are still under analysis, so that we should not wait a long time before knowing if this prediction can be confirmed.

It is important to notice that the same presence of  $^{26}\text{Al}$  in the grains, at a level higher than allowed by TDU (which therefore requires the operation of deep mixing), poses crucial constraints to the physical mechanisms driving the transport of processed matter. Contrary to what was found on the RGB, here thermohaline diffusion cannot be an explanation. Not only its effectiveness is put in doubt (or at least reduced) by the previous  $^3\text{He}$  consumption, but the layers where it starts are too cool to host any  $^{26}\text{Al}$ . This is evident in Fig. 6. On the AGB, the  $^3\text{He}+^3\text{He}$  reaction prevails over the  $^3\text{He}+^4\text{He}$  for  $\Delta \geq 0.15$ , identified in the first panel of the figure by the kink in the  $^3\text{He}$  curve. As the third panel shows, the whole abundance of  $^{26}\text{Al}$  is produced inside that zone. As we showed in Fig. 11, accounting for  $^{26}\text{Al}$  in oxide grains requires  $\Delta \leq 0.1$ . We believe this is a clear demonstration that thermohaline mixing is not the mechanism driving extra-mixing in AGB stars. Even its action as a driver of magnetic-like mechanisms (Denissenkov et al. 2009) would not be useful in this case. Completely different physical processes, like e.g. magnetic buoyancy (Busso et al. 2010) or gravitational waves (Denissenkov & Tout 2003), must necessarily be at play.

Further comparisons with observations are provided by Fig. 12. Its left panel shows

C/O and  $^{12}\text{C}/^{13}\text{C}$  measurements in both O-rich (Smith & Lambert 1990) and C-rich stars (Abia et al. 2002, 2010). The curves refer to our 1.5 and 2  $M_{\odot}$  models; the more massive case is the one that reaches  $\text{C}/\text{O} \geq 1$ ; its C-rich phases are marked by a continuous line, the O-rich ones by a dashed line. We adopted  $\Delta = 0.2$  and 0.25 and  $\dot{M}_6$  values as indicated by the labels. It is clear that the whole area of the observations is very well accounted for. This figure offers a rather global test from stars, complementing those derived from oxide grains; it confirms that the general scenario is correct and that MS, S and C stars have indeed the masses we suggested and do experience extra-mixing.

A much less satisfactory comparison is presented in the right panel of Fig. 12, where our model curves are superimposed to the the nitrogen and carbon isotopic ratios measured in SiC grains of AGB origin (see e.g. Zinner 2005; Zinner et al. 2006, and references therein). The models in the figure are labeled by the values of  $\Delta$  and  $\dot{M}_6$ . They mainly cover the area of the so-called "mainstream" SiC grains (with carbon isotopic ratios between 20 and 100), but only for the upper part of the range in  $^{14}\text{N}/^{15}\text{N}$ . Models with rather extreme  $\dot{M}_6$  values can reach the area where the grains with the lowest  $^{12}\text{C}/^{13}\text{C}$  ratios (called A & B grains) are present, but again only for very high values of  $^{14}\text{N}/^{15}\text{N}$ . These inconsistencies are not new and have characterized the attempts at explaining the nitrogen isotopes in SiC grains for many years (see e.g. Nollett et al. 2003). Notice that the two filled circles, at  $^{14}\text{N}/^{15}\text{N} = 680$  and 5300, refer to the only (very uncertain) data from red giants (Wannier et al. 1991) and confirm that the RGB ratios must indeed be much larger than solar. The low values of many SiC grains have no explanation at all in low mass stars. In principle, in the so-called  $^{13}\text{C}$ -pocket of AGB stars a reservoir of  $^{15}\text{N}$  exists. This is generated trough proton and neutron captures on  $^{14}\text{N}$  and later, at the onset of the thermal pulse, by the activation of the  $^{18}\text{O}(p,\alpha)$  reaction, see also Abia et al. (2010). However, these zones are not expected to be ejected and their  $^{15}\text{N}$  is subsequently destroyed in the convective thermal pulse.

Contamination of the grains with solar-system nitrogen seems unlikely, as there is no correlation between the  $^{15}\text{N}$  concentration and grain size, as would be expected (Zinner, private communication). A possible alternative is the contamination from cosmic ray spallation, where  $^{15}\text{N}$  is produced abundantly. In such a case the  $^{15}\text{N}$  content would be a measure of the grain age and would not inform on stellar nucleosynthesis.

## 7. Toward a physical model of deep mixing: constraints on the parameters

As a concluding remark we want to make some comments on the recent numerical simulations of extra-mixing presented by Denissenkov (2010) and by Denissenkov & Merryfield (2010). The work was performed through an analogy with current research on thermohaline processes known to occur in the oceans. The models were then extrapolated to the stellar case, on the basis of the values of physical parameters valid for red giants; this treatment has obviously a much higher degree of sophistication than in simple 1D analysis, but still includes very uncertain parameters. Anyhow, the authors suggest that the molecular weight inversion generated by  $^3\text{He}$  burning induces finger-like mixing structures whose average aspect ratio (length over diameter,  $\alpha = l/a$ ) is too small by a factor of at least 50 as compared to what observations require; this aspect ratio, squared, is proportional to the diffusion coefficient in a diffusive treatment, or to the mixing velocity in a circulation-like transport (Nollett et al. 2003). In Denissenkov (2010) it is also mentioned that, for explaining the small number of red giant stars that are very Li-rich ( $\log \epsilon(\text{Li}) \geq 1.5$ ) the aspect ratios found with thermohaline processes would be too small by a factor of several hundreds; in fact, producing  $^7\text{Li}$  is known to require a kind of transport fast enough to save to the envelope the short-lived  $^7\text{Be}$  ( $t_{1/2} = 53$  days). These results would indicate that thermohaline diffusion alone is insufficient to drive the chemical mixing required in red giants; as a way out, in Denissenkov & Merryfield (2010) it is suggested that a coupling

with magnetically-induced effects might be more promising.

The above results should now be verified by other authors, before final conclusions can be drawn. Recent works either attribute the isotopic mix of red giants to the effects of thermohaline mixing alone (Charbonnel & Zahn 2007) or confirm that models for this process find velocities that are too low by a large factor, thus opening the possibility that other mechanisms contribute (Cantiello & Langer 2010).

Although our simple parameterized approach cannot enter into such details, we found the treatment by Denissenkov (2010) and Denissenkov & Merryfield (2010) very instructive as a tool to infer the required properties of suitable physical models for extra-mixing. In particular, it was suggested (Busso et al. 2007a; Denissenkov et al. 2009) that magnetic buoyancy might offer an alternative to thermohaline diffusion, with the advantage that it would not require a nuclear process as a trigger, hence it would have a wider possibility of application (e.g. to the formation of the  $^{13}\text{C}$ -pocket). If magnetic buoyancy were to proceed through the development of  $\Omega$ -shaped loops, formed as instabilities in MHD waves (Parker 1994), then each such structure would look like a couple of mixing fingers. Let us make two illustrative examples to derive limits on the aspect ratios of these structures. As a zero-order approximation we can consider the model by Busso et al. (2007a), neglecting any slowing process (such as phase mixing or thermal exchanges, see e.g. Spruit 1999, 2002; Denissenkov et al. 2009). In this case the buoyancy velocity is close to the Alfvén velocity and the aspect ratio, for the cases discussed by Busso et al. (2007a), turns out to be in the range 200–300, suitable for Li production. Alternatively, a less efficient transport is obtained if the instabilities can travel only a limited distance  $l$  before interfering destructively (by phase mixing) with previously-detached buoyant structures. The length covered is  $l = \pi\Delta t_A/t$ , where  $t$  is the available time for the mixing and  $\Delta t_A$  is the crossing time of Alfvén waves over the star’s dimension (Spruit 1999; Busso et al. 2004). In such a

case, using the parameters of RGB phases by Busso et al. (2007a), one can easily derive that the aspect ratio becomes very small (of the order of 0.1–0.2), suitable to account for the requirements of the carbon isotopic ratios in red giants and with a correspondingly small velocity. A similarly small velocity is obtained for the magneto-thermohaline mixing by Denissenkov et al. (2009). These are only very simplified, order-of-magnitude estimates, derived just by applying to magnetic buoyancy some of the considerations by Denissenkov (2010). However, they are already sufficient to underline that this kind of mechanism deserves now to be carefully modeled, as it seems to be able to cover the whole range of mixing velocities (or aspect ratios) required by virtually all the chemical peculiarities displayed by red giant stars.

## 8. Conclusions

In this paper we presented revised parametric calculations of nucleosynthesis in extra-mixing phenomena occurring in low mass evolved stars, from the phase of the FDU up to the end of the AGB stage. The calculations were based on a recent revision of the FRANEC code and on a new extra-mixing code. They incorporated several physical and numerical improvements, among which new opacities for carbon-rich envelopes, a new algorithm for the determination of the convective border position, and a new mass-loss law.

With these tools we explored the coupling of nucleosynthesis and non-convective mixing in RGB and AGB phases, comparing the results obtained with the old NACRE compilation of reaction rates with those descending from the adoption of new recommendations from ADE10 and ILI10. In particular, the specific choices made for each updated reaction rate were commented extensively in the Appendix.

It was found that, among the new reaction rates, the ones inducing the largest

variations in the evolution of LM stars are those for proton captures on  $^{14}\text{N}$  and (to a lesser extent) for proton captures on  $^{17}\text{O}$ . Similar conclusions were recently obtained in another context by Magic et al. (2010). We obtained huge changes in the oxygen isotopic composition of the envelope, starting from FDU. Their effects include a drastic shrinking of the mass interval in which AGB stars can produce oxide grains like those recovered in pristine meteorites. Most such grains appear to come from stars below  $1.5 M_{\odot}$ . Another important revision of previous knowledge was the discovery that all  $^{18}\text{O}$ -poor grains (those with  $^{18}\text{O}/^{16}\text{O}$  below 0.0015) can now be explained, without the "forbidden regions" previously found for the lowest  $^{17}\text{O}/^{16}\text{O}$  ratios. Concerning the evolution of AGB stars of low mass and solar metallicity we suggested that most MS, S stars should have masses below  $1.5 - 1.7 M_{\odot}$ ; in this mass interval they would never produce C-stars, also thanks to  $^{12}\text{C}$  processing in deep mixing.

Constraints coming from observations of CNO nuclei in both RGB and AGB stars were well reproduced by deep mixing models with the new rates. In particular, for RGB stars we found that extra-mixing processing does not need to penetrate to very high temperatures, so that thermohaline diffusion might be an adequate scenario for those phases, if the problems recently mentioned in the literature for its too low diffusion coefficients can be solved. We then confirmed that deep mixing is required also on the AGB. In this case, the abundances of  $^{26}\text{Al}$  in presolar grains indicate that the transport must reach much hotter layers than in RGB stages. This fact (and the previous consumption of  $^3\text{He}$ ) induced us to conclude that thermohaline diffusion is not a viable explanation for the transport processes occurring in the latest evolutionary stages. The existence of a small population of oxide grains with low  $^{17}\text{O}/^{16}\text{O}$  and high  $^{26}\text{Al}/^{27}\text{Al}$  ratios was suggested to require some further revision of the rates for  $^{26}\text{Al}$  synthesis at low temperatures, probably an increase for the  $^{25}\text{Mg}(p,\gamma)^{26}\text{Al}$  rate.

The longstanding impossibility of accounting for the whole range of the nitrogen isotopic ratios in SiC grains remains unchanged after our work. It was argued that no stellar process occurring in low mass stars can solve this problem and that SiC grains might be contaminated by cosmic ray spallation processes in the interstellar medium.

We are indebted to many colleagues for helping us in the understanding of the subtleties of low mass star nucleosynthesis. While recognizing the role of all of them is impossible, we cannot avoid acknowledging the fundamental lessons we learned from friends like G.J. Wasserburg, R. Gallino, O. Straniero and K.M. Nollett. M.L. acknowledges the support of the Italian Ministry of Education, University and Research under Grant No. RBFR082838 (FIRB2008)

## A. The choice of nuclear reaction rates

### A.1. The reactions $^{14}\text{N}(p, \gamma)^{15}\text{O}$ and $^{15}\text{N}(p, \gamma)^{16}\text{O}$ .

The  $^{14}\text{N}(p, \gamma)^{15}\text{O}$  reaction is the slowest reaction of the CN cycle, hence the one determining the duration of the process. The low-energy cross section is dominated by a resonance at 259 keV. In particular, at the temperatures of interest here ( $T_9 \lesssim 0.06$ ), the reaction rate mainly depends on the resonance tail, the Gamow window extending (at most) to around 110 keV. Such a region is only partly covered by experimental data, spanning energies as low as 70 keV, so the S-factor is very sensitive to the extrapolating curve and can be severely affected by the  $-504$  keV subthreshold resonance. In the last years, direct measurements (in both surface and underground laboratories) and indirect measurements (Doppler shift attenuation, Coulomb excitation, Asymptotic Normalization Constant) have been performed, primarily triggered by the discovery that the contribution of the ground-state transition had been previously overestimated. From these measurements,



ADE10 recommend  $S(0) = 1.66 \pm 0.12$  keV b, which is about half the NACRE value  $S(0) = 3.2 \pm 0.8$  keV b. This entails a significantly lower reaction rate in the range of our interest, as shown in Fig. 13, left panel.

The  $^{15}\text{N}(p, \gamma)^{16}\text{O}$  reaction fixes the leak rate from the CN-cycle to the CNO bi-cycle. Besides the direct capture contribution, the cross section is characterized by the interference of two  $1^-$  resonances at 312 and 964 keV. As for  $^{14}\text{N}(p, \gamma)^{15}\text{O}$ , the largest energy of interest is  $\sim 110$  keV, thus the extrapolation procedure is critical. In NACRE, a very large  $S(0)$  was obtained ( $64 \pm 6$  keV b) while ADE10 recommend  $36 \pm 6$  keV b following the results from an underground measurement (which does not cover the Gamow window anyway) and an ANC measurement, yielding an absolute value of the direct-capture contribution ten times smaller than NACRE. Consequently, a 30-40% smaller reaction rate is now obtained in the temperature region we are dealing with (Fig. 13, right panel), by using the low-energy  $S(E)$ -factor recommended by ADE10.

### A.2. The reactions $^{16}\text{O}(p, \gamma)^{17}\text{F}$ , $^{17}\text{O}(p, \gamma)^{18}\text{F}$ , and $^{17}\text{O}(p, \alpha)^{14}\text{N}$ .

The operation of the  $^{16}\text{O}(p, \gamma)^{17}\text{F}$  reaction contributes to establish the ratios of oxygen isotopes in red giants and plays therefore a major role in the analysis of oxygen-rich presolar grains of circumstellar origin. At the energies of interest for this work, and up to  $\sim 120$  keV, the cross section is determined by the direct capture to the ground and first excited states of  $^{17}\text{F}$ . Direct measurements exist down to about 100 keV, so extrapolations are needed. In the previous evaluation by NACRE, the greatest part of the error was attributed to the model assumed in the calculation. Improved calculations have now reduced the uncertainty affecting the  $S(0)$  parameter, from 30% to 7.5% (see ADE10 for details), while the recommended value is in substantial agreement with the one from NACRE. Fig. 14 (left panel) shows the resulting reaction rate.

Much like the previously-mentioned reaction, also  $^{17}\text{O}(p, \gamma)^{18}\text{F}$  is expected to modify the relative abundances of oxygen isotopes. In the  $E_{cm} \lesssim 120$  keV energy range, the cross section shows a resonance at 65.1 keV that strongly influences the reaction rate above  $T_9 = 0.02$ . At lower temperatures, the dominant role is played by direct captures, while the subthreshold resonance at -3.1 keV does not provide any significant contribution. The 65.1 keV resonance and the direct capture term have been the subject of several improved calculations, leading to a change in the resonance energy (it was 66 keV in NACRE) and in its strength (which is a factor  $\sim 3.7$  smaller than given in NACRE). Concerning the direct-capture contributions, the revised calculations yield a  $\sim 30\%$  smaller  $S(E)$  factor below 120 keV, which is responsible for the reduced reaction rate below  $T_9 = 0.02$ , as shown in Fig. 14, central panel.

The  $^{17}\text{O}(p, \alpha)^{14}\text{N}$  competes with the  $^{17}\text{O}(p, \gamma)^{18}\text{F}$  channel, removing  $^{17}\text{O}$  nuclei and turning the nucleosynthesis path back towards nitrogen. In contrast with the radiative capture channel, the  $-3.1$  keV subthreshold resonance gives a major contribution to the reaction rate for  $T_9 < 0.02$ . Updated calculations for these resonances are given in both the reviews we are considering. In particular, the  $-3.1$  keV-state proton width is lowered by a factor  $\sim 3$  as compared to NACRE. No expression for the reaction rate is given in ADE10; hence we use the reaction rate table in ILI10, extrapolating down to the  $T_9 = 0.004 - 0.01$  temperature range. A remarkably lower reaction rate is thus obtained (see Fig. 14, right panel). Regarding the  $^{18}\text{O}(p, \alpha)^{18}\text{N}$  reaction, despite the extensive experimental investigation in the last years (ADE10, ILI10, La Cognata et al. 2008, 2010b) has produced a significant change in the recommended reaction rate (about 30%) and a reduction of its uncertainty (about a factor of 8) at low temperatures, its effect on AGB nucleosynthesis turns out to be negligible. The updated reaction rate has been included anyway in the present work.

### A.3. The $^{20}\text{Ne}(p, \gamma)^{21}\text{Na}$ , $^{21}\text{Ne}(p, \gamma)^{22}\text{Na}$ and $^{22}\text{Ne}(p, \gamma)^{23}\text{Na}$ reactions

The  $^{20}\text{Ne}(p, \gamma)^{21}\text{Na}$  reaction is the starting point of the NeNa cycle and plays a key role, being the slowest reaction of the cycle. Inside the Gamow window, extending up to  $\sim 130$  keV, the astrophysical factor is dominated by a subthreshold resonance laying at about -7 keV. Additional 8 resonances show up at higher energies (up to about 2 MeV). In ADE10 both the resonance excitation energy and its strength have been re-evaluated using more recent measurements, resulting in a small increase of the  $S(E)$ -factor, by 2.9%. Moreover, a new fit of the energy trend for the  $S(E)$ -factor has been provided for the numerical integration of the reaction rate. The resulting rate is displayed in Fig. 15, left panel, which shows a substantial agreement with the NACRE one and a slightly reduced uncertainty.

For the  $^{21}\text{Ne}(p, \gamma)^{22}\text{Na}$  reaction, we adopt the recommendation by ILL10. They make use of nuclear-physics input parameters from Iliadis et al. (2001). Resonances were measured for  $E_{cm} \geq 121$  keV, corresponding to the upper edge of the Gamow window. Two threshold states, corresponding to resonance energies of  $E_{cm} = 17$  and 95 keV, have been considered. While the latter (for which only an upper limit of the spectroscopic factor is known) adds a negligible uncertainty to the reaction rate, the former can influence it at low temperatures (below  $T_9 \sim 0.02$ ). Though the reaction-rate accuracy has been improved with respect to NACRE around  $T_9 \sim 0.03$ , for  $T_9 \lesssim 0.02$  the total rate remains uncertain by several orders of magnitude (see Fig. 15, central panel).

The rate of the  $^{22}\text{Ne}(p, \gamma)^{23}\text{Na}$  reaction is taken from ADE10 and is shown in Fig. 15, right panel. The main difference with respect to previous compilations is the treatment of the threshold states. Concerning the 151-keV resonance, its spectroscopic factor has been considered as a mean value rather than an upper limit. Lower energy resonances, whose existence had been considered as tentative, were disregarded by ADE10. As a result,

the recommended rate is smaller than in NACRE above  $T_9 \sim 0.03$ , but remains in good agreement with the previous indications elsewhere. The error has been instead significantly reduced.

#### A.4. The $^{23}\text{Na}(p, \gamma)^{24}\text{Mg}$ and $^{23}\text{Na}(p, \alpha)^{20}\text{Ne}$ reactions

The Gamow window of the  $^{23}\text{Na}(p, \gamma)^{24}\text{Mg}$  reaction extends up to about 140 keV. Therefore, the main contribution to the low-temperature reaction rate is due to the threshold states. ILI10 mostly make use of the updated nuclear physics input parameters by Hale et al. (2004) in this energy region, which have been indirectly measured by means of  $(^3\text{He}, d)$  transfer reactions. The contribution of direct capture to the cross section has been taken from the same work. The resulting reaction rate is compared with the NACRE choice in Fig. 16 (left panel). The updated value lays well within the upper and lower limits set by NACRE, although the uncertainty is greatly reduced.

Concerning the  $^{23}\text{Na}(p, \alpha)^{20}\text{Ne}$  reaction, the same considerations as for the  $^{23}\text{Na}(p, \gamma)^{24}\text{Mg}$  can be repeated. The resulting reaction rate is given in Fig. 16, right panel. The new rate is about 100 times smaller than the one recommended by NACRE at the lowest temperatures, while the uncertainty is significantly smaller.

#### A.5. The reactions $^{24}\text{Mg}(p, \gamma)^{25}\text{Al}$ , $^{25}\text{Mg}(p, \gamma)^{26}\text{Al}_{gs}$ , $^{25}\text{Mg}(p, \gamma)^{26}\text{Al}_m$ , $^{26}\text{Mg}(p, \gamma)^{27}\text{Al}$ .

The  $^{24}\text{Mg}(p, \gamma)^{25}\text{Al}$  reaction influences the nucleosynthesis of magnesium and aluminum, which are key elements in the analysis of ancient meteorites and presolar grains. No experimental data are available inside the Gamow window (which extends up to  $E_{cm} \sim 150$  keV). The most recent measurements provide the cross section down to 200 keV (see ILI10 and reference therein), where 9 resonances occur (up to 2.3 MeV). In the review by

ILI10, the reaction rate is calculated from the these data, including re-normalizations of the strengths of higher-energy resonances and updated Q-values. Moreover, with respect to the NACRE compilation, a more reliable direct capture contribution to the  $S(E)$  factor has been estimated, as well as the contribution of the 214 and 402 keV resonance tails, by means of numerical integrations. Despite all these improvements, the resulting reaction rate (Fig. 17, left panel) is in overall fair agreement with the NACRE recommendations. It is shown for  $T_9 > 0.01$ , but the reaction rate is there  $\sim 10^{-35} \text{cm}^3 \text{mol}^{-1} \text{s}^{-1}$ , so that the  $^{24}\text{Mg}(p, \gamma)^{25}\text{Al}$  reaction does not contribute to nucleosynthesis at very low energies.

As for the previous case, the  $^{25}\text{Mg}(p, \gamma)^{26}\text{Al}_{gs}$  reaction (where "gs" stands for "Ground State") is important for us to understand the magnesium and aluminum nucleosynthesis in evolved red giants. Data exist in a wide energy range, starting from 37 keV and extensively overlapping with the Gamow peak. Concerning the nuclear physics inputs, the differences of the ILI10 review with respect to NACRE are: (i) the use of re-normalized strengths for resonances above  $E_{cm} = 189$  keV; (ii) the adoption of the more accurate ground-state  $\gamma$ -ray branching ratios  $f_0$  for the 189, 244 and 292 keV resonances; and (iii) a new calculation of the contribution of the 37 keV resonance. The reaction rate is displayed in Fig. 17, right panel: the recommended value is in good agreement with NACRE, but the uncertainty has been reduced by more than a factor of 2 at the lowest temperatures that are most important for us.

The same considerations done above apply to the  $^{25}\text{Mg}(p, \gamma)^{26}\text{Al}_m$  reaction (where "m" indicates the isomeric meta-stable state), but in addition the isomeric-state  $\gamma$ -ray branching ratio  $1 - f_0$  has been taken into account. Once again, while the recommended value by ILI10 is in overall agreement with NACRE, the uncertainties are reduced by more than a factor of 2 at the temperatures of AGB stars (Fig. 18, left panel)

For the  $^{26}\text{Mg}(p, \gamma)^{27}\text{Al}$  reaction, Fig. 18 (right panel) shows a remarkable difference

between the updated reaction rate by ILI10 and the NACRE value, ranging from a factor of 2 up to 8, while the error has been reduced, especially at high temperatures. Indeed, a different direct-capture component was adopted, the strengths of the measured resonances (above  $E_{cm} \sim 100$  keV) were re-normalized and the contributions of the lower-energy resonances at  $E_{cm} = 53$  keV and  $E_{cm} = 105$  keV were re-analyzed. One has to remark that some ambiguity on the assignment of quantum numbers for these levels still exists (see ILI10 for a more detailed discussion).

#### A.6. The reactions $^{26}\text{Al}(p, \gamma)^{27}\text{Si}$ , $^{27}\text{Al}(p, \gamma)^{28}\text{Si}$ , and $^{27}\text{Al}(p, \alpha)^{24}\text{Mg}$ .

The  $^{26}\text{Al}(p, \gamma)^{27}\text{Si}$  reaction is important for establishing the equilibrium abundance of the radioactive isotope  $^{26}\text{Al}$ , playing a major role in presolar grain studies,  $\gamma$ -ray astronomy and solar system formation (see e.g. Busso 2010; Busso et al. 2003; Wasserburg et al. 2006, for this last point). Fig. 19 (left panel) shows that the updated reaction rate by ILI10 lays within the fiducial interval by NACRE, but at low temperature the recommended value is strongly decreased. Also the uncertainty has been greatly reduced. In the estimate of the reaction rate, ILI10 introduced a calculated direct-capture component and the contribution of 19 resonances. In particular, for almost all resonances below  $E_{cm} \sim 500$  keV, the resonance energies were computed from updated excitation-energy determinations, while improved calculations of the proton widths of unobserved low-energy resonances were used to evaluate their contribution to the rate.

For the  $^{27}\text{Al}(p, \gamma)^{28}\text{Si}$  reaction, ILI10 made use of the nuclear physics input parameters reviewed in Iliadis et al. (2001). With respect to the NACRE compilation, the direct-capture contribution was recalculated, the strengths of the measured resonances were re-normalized (above  $E_{cm} \sim 200$  keV, to be compared with the upper limit of the Gamow window,  $\sim 160$  keV) and the contribution of four sub-threshold resonances were re-evaluated (the

most important are at  $E_{cm} = 72$  keV and  $E_{cm} = 85$  keV). In particular, an improved determination of their spectroscopic factors was performed, based on the re-analysis of the  $^{27}\text{Al}(^3\text{He}, d)^{28}\text{Si}$  stripping data. Consequently, the recommended total rate deviates from NACRE up to a factor of 20 in the energy range common to AGB stars (Fig. 19, central panel), mainly because of improved estimates of spectroscopic factors for the threshold states.

A total of 91 resonances at energies of  $E_{cm} = 72 - 2966$  keV were taken into account by ILI10 for calculating the reaction rate for the process  $^{27}\text{Al}(p, \alpha)^{24}\text{Mg}$ . For the measured resonances (for  $E_{cm} \gtrsim 486$  keV), the same nuclear physics input parameters considered in Iliadis et al. (2001) were adopted. The same holds for threshold resonances, whose strengths were calculated from a re-analysis of the  $^{27}\text{Al}(^3\text{He}, d)^{28}\text{Si}$  stripping cross section and from spectroscopic data in the literature (see ILI01 and references therein). The improved estimates of spectroscopic factors for the threshold states, as in the  $^{27}\text{Al}(p, \gamma)^{28}\text{Si}$  case, determine an increase of the recommended total rate with respect to NACRE by a factor of 10 (Fig. 19, right panel).

Finally, we recall that  $(p, \gamma)$  and  $(p, \alpha)$  captures on fluorine have not been addressed by either ADE10 or ILI10. However, recent measurements (Couture et al. 2007; Spyrou et al. 2000) only confirmed previous suggestions, so that the rates do not require updates, and we adopt them from NACRE.

## REFERENCES

- Abia, C., Busso, M., Gallino, R., et al. 2001, *ApJ* 559, 1117
- Abia C., Domínguez I., Gallino R., et al. 2002, *ApJ* 579,817
- Abia, C., Cunha, K., Cristallo, S., et al. 2010, *ApJ* 715, 94
- Adelberger, E.G., Austin, S.M., Bahcall, J.N., et al. 1998, *Rev. Mod. Phys.* 70, 1265
- Adelberger, E.G., Balantekin, A.B., Bemmerer, D., et al. 2010, arXiv1004, 2318
- Amari, S., Nittler, L.R., Zinner, E., Gallino, R., Lugaro, M., & Lewis, R.S. 2001, *ApJ* 546, 248
- Andrews, A.D., Rodono, M., Linsky, J.L., et al. 1998, *A&A* 204, 177
- Anders, E., & Grevesse, N. 1989, *Geochim. Cosmochim. Acta* 53, 197
- Angulo, C., Arnould, M., Rayet, M., et al. 1999, *Nucl. Phys. A* 656, 3
- Asplund, M., Grevesse, N., Sauval, J., & Scott, P. 2009, *ARA&A*, 47, 481
- Bania, T.M., Rood, R.T., Balser, D.S. 2002, *Nature* 415, 54
- G. Baur, & H. Rebel 1994, *J. Phys. G* 20, 1
- Beard, M., Afanasjev, A.V., Chamon, L.C., Gasques, L.R., Wiescher, M., Yakovlev, D.G. 2010, *ADNDT* 96, 54
- Brown, J.A. 1987, *ApJ* 317, 701
- Boothroyd, A.I., & Sackmann, I.-J. 1999, *ApJ* 510, 232
- Boothroyd, A.I., Sackmann, I.-J., & Wasserburg, G.J. 1994, *ApJ* 430, L77



- Busso, M., & Gallino, R. 1985, A&A 151, 205
- Busso, M., Gallino, R., & Wasserburg, G.J. 1999, ARA&A 37,239
- Busso, M., Gallino, R. & Wasserburg, G.J. 2003, PASA 20, 356
- Busso, M., Nucci, M.C., Chieffi, A., & Straniero, O. 2004, MemSAIt 75, 648
- Busso, M., Wasserburg, G.J., Nollett, K.M., & Calandra A. 2007, ApJ 671, 802
- Busso, M., Guandalini, R., Persi, P., Corcione, L., & Ferrari-Toniolo, M. 2007, AJ 133, 2310
- Busso, M. 2010, *The Early Solar System*, Lecture Notes in Physics 812, ed. R. Diehl, D.H. Hartmann and N. Prantzos, (Springer: Berlin), P. 307-342
- Busso, M., Palmerini, S., Maiorca, E., et al. 2010, ApJ 717, L47
- Cantiello, M. & Langer, N. 2010, A&A 521, 9
- Charbonnel, C. 1994, in *Origin and Evolution of the Elements*, Ed. A. McWilliam and M. Rauch (Cambridge University Press: Cambridge) 60.
- Charbonnel, C. 1995, ApJ 453, L41.
- Charbonnel, C. 1996, ASPC 109, 677
- Charbonnel, C. 2004, in *Origin and Evolution of the elements*, ed. A. McWilliams and M. Rauch, (Pasadena: Carnegie Observatories)
- Charbonnel, C. & Balachandran, S. C. 2000, A&A 359, 563
- Charbonnel, C. & Do Nascimento, J.D. Jr. 1998, A&A, 336, 915
- Charbonnel, C. & Lagarde, N. 2010, arXiv1006.5359
- Charbonnel, C. & Zahn, J.-P., 2007, A&A 467, L15

- Chieffi, A., Limongi, M., & Straniero, O. 1998, ApJ 502, 737
- Choi, B.-G., Huss, G.R., Wasserburg, G. J., & Gallino, R. 1998, Science 282, 1284
- Cottrell, P.L. & Sneden, C. 1986, A&A 161, 314
- Couture, A., Beard, M., Couder, M., et al. 2008, Phys.Rev.C 77, 015802 Department of Physics, University of Toronto, Toronto,
- Cristallo, S., Straniero, O., Lederer, M.T., & Aringer, B. 2007, ApJ 667, 489
- Cristallo, S., Straniero, O., Gallino, R., et al. 2009, ApJ 696, 797
- Cristallo, S., Piersanti, L., Straniero, O., et al. 2009, PASA 26, 139
- Cristallo, S., Straniero, O., Gallino, R., et al. 2009, MemSAIt 80, 157
- Cristallo, S., et al. (in preparation)
- Denissenkov, P.A. 2010, ApJ 723, 563
- Denissenkov, P.A., & Merryfield, W.J. 2010, arXiv:1011.2191
- Denissenkov, P.A. & Merryfield, W.J., arXiv1011.2191
- Denissenkov, P.A., Da Costa, G.S., Norris, J.E., & Weiss, A. 1998, A&A 333, 926
- Denissenkov, P. A. & Weiss, A. 1996, A&A 308, 773
- Denissenkov, P.A. & Weiss, A. 2000, 358, L49
- Denissenkov, P. A. & Tout, C. A 2003, MNRAS 340, 722
- Denissenkov, P.A., Pinsonneault, M., & MacGregor, K.B. 2009, ApJ 696, 1823
- Domínguez, I., Abia, C., Straniero, O., Cristallo, S., & Pavlenko, Ya.V. 2004, A&A 422, 1045

- Eggleton, P.P., Dearborn, D.S.P., & Lattanzio J.C. 2006, *Sci* 314, 1580
- Eggleton, P.P, Dearborn, D.S.P., & Lattanzio, J.C. 2008, *ApJ* 677, 581
- Eggenberger, P., Maeder, A., & Meynet, G. 2005, *A&A* 440, L9
- Fouchet, T., Lellouch, E., Bézard, B., et al. 2000, *Icarus* 143, 223
- Fouchet, T., Irwin, P.G.J., Parrish, P. et al. 2004, *Icarus* 172, 50
- Friel, E.D., Jacobson, H.R., & Pilachowski, C.A. 2010, *AJ* 139, 1942
- Gilroy, K.K. & Brown, J.A. 1991, *ApJ* 371, 578
- Glöcker, G., & Geiss, J. 1998, *Space Sci Rev.* 84, 273
- Gratton, R.G., Carretta, E., Eriksson, K., & Gustafsson, B. 2000, *A&A* 354, 169
- Gratton, R.G., Bonifacio, P., Bragaglia, A., Carretta, E., Castellani, V., Centurion, M.,  
Chieffi, A. et al. 2001, *A&A* 369, 87
- Grundahl, F., Briley, M., Nissen, P. E., & Feltzing, S. 2002, *A&A* 395, 481
- Guandalini, R., Busso, M., Ciprini, S., Silvestro, G., & Persi, P. 2006, *A&A* 445, 1069
- Guandalini, R. & Busso, M. 2008, *A&A* 488, 675
- Guandalini, R., Palmerini, S., Busso, M., & Uttenthaler, S. 2006, *PASA* 26, 168
- Hale, S.E. et al. 2004, *Phys. Rev.* C70, 045802
- Harris, J.H., Lambert, D.L., & Smith V.V. 1985, *ApJ* 299, 375
- Herpin, F., Baudry, A., Thum, C., et al. 2006, *A&A* 450, 667
- Herwig, F. 2005, *ARA&A* 43, 435

- Herwig, F. Pignatari, M., Woodward, P.M. et al. 2010, ApJ (in press)
- Iben, I.Jr. & Renzini, A. 1983, ARA&A 21, 271.
- Iliadis, C., Buchmann, L., Endt, P. M., Herndl, H., & Wiescher, M. 1996, Phys. Rev. C. 53, 475.
- Iliadis, C., D’Auria, J.M., Starrfield, S., Thompson, W.J., & Wiescher, M. 2001, ApJS 134, 151
- Iliadis, C., Angulo, C., Descouvemont, P., Lugaro, M., & Mohr, P. 2008, Phys. Rev. C. 77, 045802
- Iliadis, C., Longland, R., Champagne, A.E., Coc, A., & Fitzgerald, R. 2010, Nucl. Phys. A 841, 31
- Imbriani, G., Costantini, H., Formicola, A., et al. 2005, EPJ A 25, 455
- Käppeler, F., Wiescher, M., Giesen, U., et al. 1994, ApJ 437, 396
- Kippenhahn, R., & Weigert, A. 1990, Stellar Structure and Evolution (Springer: Berlin)
- La Cognata, M., et al. 2008, Phys Rev Lett 101, 152501
- La Cognata, M., et al. 2010, APJ, 708, 796
- La Cognata, M., et al. 2008, J. Phys. G: Nucl. Part. Phys., 35, 014014
- Lemut, A., Bemmerer, D., Confortola, F. et al. 2006, Phys. Lett. B. 634, 483
- Lodders, K. 2003, ApJ 591, 1220
- Lugaro, M., Herwig, F., Lattanzio, J. C., Gallino, R., Straniero, O. 2003, APJ, 586, 1305.
- Magic, Z., Serenelli, A., Weiss, A., Chaboyer, B. 2010, ApJ, 718, 1378

- Maeder, A. & Meynet, G. 2004, in *Evolution of Massive Stars with Rotation*
- Meléndez, J., & Cohen, J.G. 2009, *ApJ* 699, 2017
- Mikolaitis, Š., Tautvaišiene, G., Gratton, R. et al. 2010, *MNRAS* (in press)
- Mukhamedzhanov, A. M., et al. 1997, *Phys. Rev. C* 56, 1302
- Nittler, L.R., Alexander, C.M.O'D., Gao, X., Walker, R.M., & Zinner, E. 1997, *Nucl. Phys.*  
A 621, 113
- Nittler, L.R., Alexander, C.M.O'D., Gallino, R., et al. 2008, *ApJ* 682,1450
- Nollett, K.M., Busso, M., & Wasserburg, G.J. 2003, *ApJ* 582, 1036
- Nordhaus, J., Busso, M., Wasserburg, G.J. et al. 2008, *ApJ* 684, L29
- Owen, T., Mahaffy, P.R., Niemann, H.B., Atreya, S., & Wong, M. 2001, *ApJ* 553, L77
- Palacios, A., Charbonnel, C., Talon, S., & Siess, L. 2006, *A&A*, 453, 261
- Palmerini, S., Nollett, K., & Busso, M. 2008, 10th Symposium on Nuclei in the Cosmos  
(<http://pos.sissa.it/cgi-bin/reader/conf.cgi?confid=53>)
- Palmerini, S., Busso, M., Maiorca, E., & Guandalini, R. 2009, *PASA* 26, 161
- Pancino, E., Carrera, R., Rossetti, E., & Gallart, C. 2010, *A&A* 511, 56
- Parker, E.N. 1994, *ApJ* 433, 867
- Pignatari, M., Gallino, R., Heil, M., Wiescher, M., Kppeler, F., Herwig, F., & Bisterzo, S.  
2010, *ApJ* 710, 16557
- Pilachowski, C., Sneden, C., Freeland, E., & Casperson, J. 2003, *AJ*, 125, 794
- Prada Moroni, P.G., Straniero, O., De Marchi, G., & Paresce, F 2004, *MemSAIt* 75, 81

- Raiteri, C. M., Gallino, R., Busso, M., Neuberger, D., & Kaeppler, F. 1993, ApJ 419,207
- Ramírez, S.V., & Cohen, J.G. 2002, AJ 123, 3277
- Randich, S., Sestito, P., Primas, F., Pallavicini, R., & Pasquini, L. 2006, A&A 450, 557
- Richard, O., Michaud, G., & Richer, J. 2005, ApJ 619, 538
- Sedlmayr, E. 1994, Lecture Notes in Physics, 428, 163
- Shetrone, M.D., Sneden, C., & Pilachowski, C.A. 1993, PASP 105, 686
- Smiljanic, R., Gauderon, R., North, P., Barbuy, B., Charbonnel, C., & Mowlavi, N., A&A 502, 267
- Smith, V.V., & Lambert, D.L. 1990, ApJSS 72, 387
- Sneden, C., Cowan, J.J., Gallino, R. 2008, ARA&A, 46, 241.
- Spiegel, E.A. 1972, ARA&A 10, 261
- Spiegel, E.A., & Zahn, J.P. 1992, A&A 265, 106
- Spruit, H.C. 1999, A&A 349, 189
- Spruit, H.C. 2002 A&A 381, 923
- Spyrou, K., Chronidou, C., Harissopulos, S., et al. 2000, Eur. Phys. J. A 7, 79
- Straniero, O., Chieffi, A. Limongi, M., et al. 1997, ApJ 478, 332
- Straniero, O., Domínguez, I., Cristallo, S. et al. 2003, PASA 20, 389
- Straniero, O, Gallino, R., & Cristallo, S. 2006, Nucl. Phys. A 777, 311
- Sweigart, A.V., & Mengel, J.G. 1979, ApJ 229 624

- Stothers R. & Simon, N.R. 1969, ApJ 157, 673
- Tautvaišiene, G., Edvardsson, B., Tuominen, I., & Ilyin, I. 2000, A&A 360, 499
- Thévenin, F., Charbonnel, C., de Freitas Pacheco, J.A., et al. 2001, A&A 373, 905
- Vassiliadis, E., & Wood, P.R. 1993, ApJ 413,641
- van Winckel, H. 2003, ARA&A 41, 391
- Ulrich, R.K. 1972, ApJ 172, 165
- Wannier, P.G., Andersson, B.-G., olofsson, H., Ukita, N., & Young, K. 1991, ApJ 380, 593
- Wasserburg, G.J., Boothroyd, A.I., & Sackmann, I.-J. 1995, ApJ 447, L37
- Wasserburg, G.J., Busso, M., Gallino, R., & Nollett, K.M. 2006, Nucl. Phys. A. 777, 5.
- Weiss, A., Denissenkov, P.A., & Charbonnel, C. 2000, 356, 181
- Yong, D., Grundahl, F., Nissen, P.E., Jensen, H.R., & Lambert, D.L. 2005, A&A 438, 875
- Zahn, J.-P. 1992, A&A, 265, 115
- Zahn, J.-P. 1992, A&A, 228, 829
- Zinner, E.K. 2005, in *Treatise of Geochemistry I. Meteorites, Comets, and Planets*, ed. A.M. Davis, (Elsevier: Amsterdam), p. 17
- Zinner, E.K., Nittler, L.R., Gallino, R., et al. 2006, ApJ 650, 350

## Figures



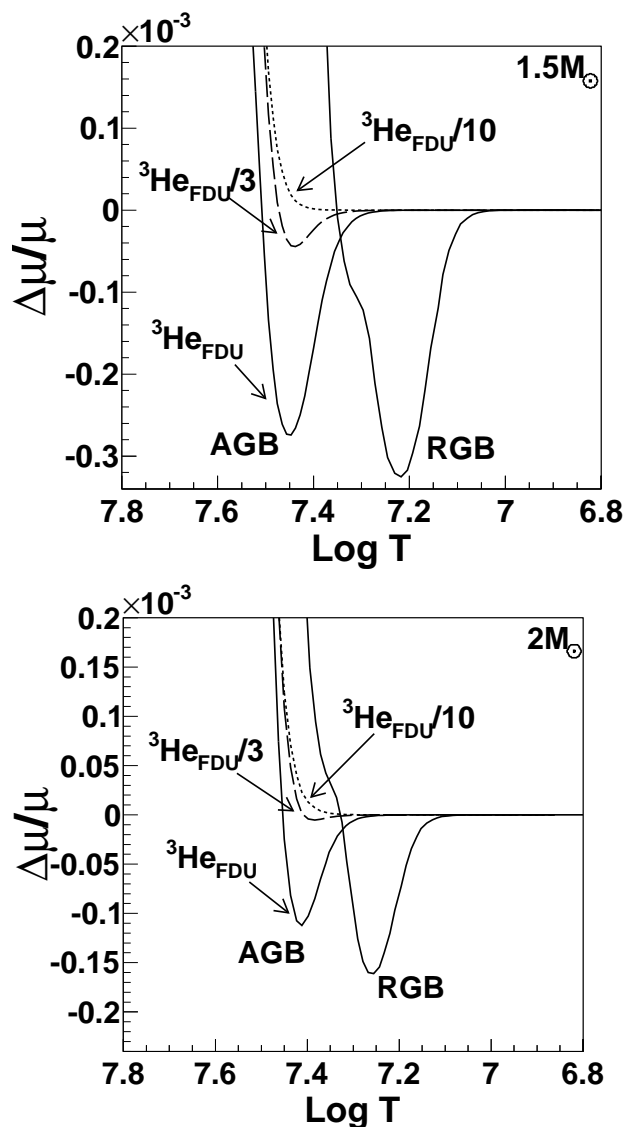


Fig. 1.— Relative variation of the molecular weight ( $\Delta\mu/\mu$ ) for a 1.5 and a 2.0  $M_{\odot}$  star with solar metallicity, in the layers hosting  ${}^3\text{He}$  burning above the H shell. The  $\mu$  inversion, present on the RGB, is preserved also on the AGB only if a sufficient supply of  ${}^3\text{He}$  remains. For the AGB, different lines refer to different abundances of  ${}^3\text{He}$  resulting from the previous RGB phase, as indicated by the labels.

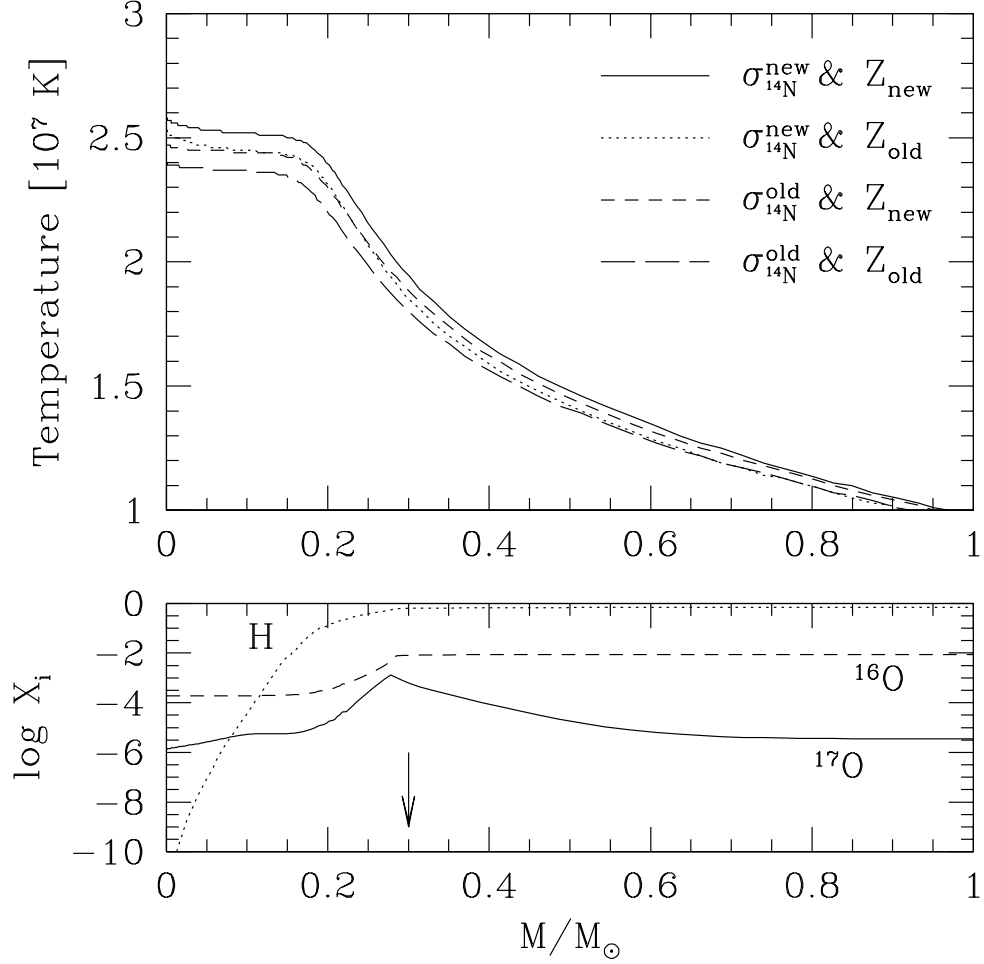


Fig. 2.— Upper panel: the profile of the stellar temperature as a function of the fractional mass at central H exhaustion in a model star of  $2 M_{\odot}$ , run with the indicated choices of the reaction rate for proton captures on  $^{14}\text{N}$  and of the solar metallicity.  $Z_{\text{new}}$  and  $Z_{\text{old}}$  refer to the values reported by Asplund et al. (2009) and Anders & Grevesse (1989), respectively. Lower panel: the  $^{16}\text{O}$  and  $^{17}\text{O}$  abundance profiles at the same moment to which panel 1 refers. The plot is for our standard case (i.e. has the new  $^{14}\text{N}(p,\gamma)^{15}\text{O}$  reaction rate and the new solar metallicity). The arrow indicates the layer reached by FDU.

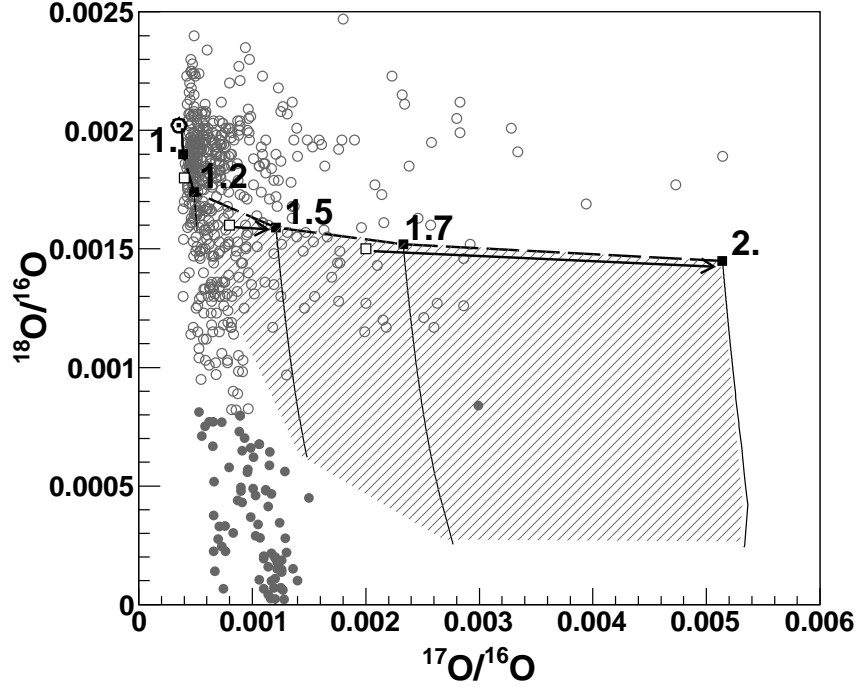


Fig. 3.— The oxygen isotopic mix in the envelope of our solar-metallicity stars at FDU (solid line). Full squares indicate the mass of the model star. As a comparison, open symbols (see arrows for associations) show the composition for the masses 1.2, 1.5 and 2  $M_{\odot}$  in the old scenario with NACRE rates and with the solar metallicity from Anders & Grevesse (1989). Dashed lines (and the corresponding shaded area) show the range of values covered by deep mixing on the RGB, for  $\Delta = 0.15$  and  $\dot{M}_6 = 0.3$ . These are rather extreme values of the parameters for the RGB phase, aimed at showing the maximum effects. The grey data points refer to measurements in presolar grains (Choi et al. 1998; Nittler et al. 1997, 2008, WUSTL Presolar Database <http://presolar.wustl.edu/pgd/>). We plot those of group 1 (open circles) and of group 2 (filled circles). The solar symbol shows the initial isotopic mix. It is clear that extra-mixing on the RGB, even operating with extreme efficiency, does not suffice to explain the data of group 2 grains.

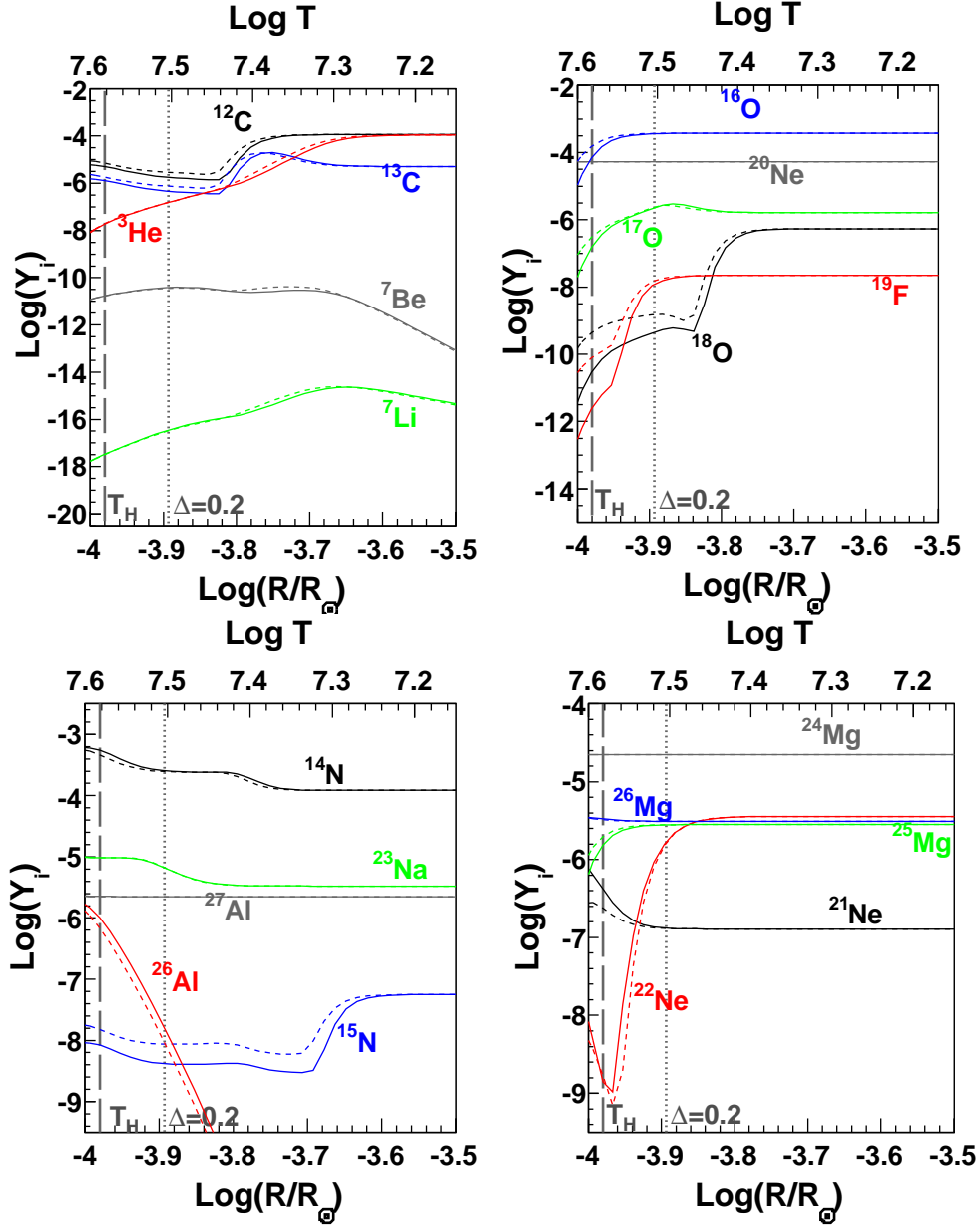


Fig. 4.— Distribution of abundances for some light and intermediate-mass isotopes in the radiative layers between the H-burning shell and the convective envelope. The plots are taken shortly after the moment when shell-H burning reaches the regions homogenized by FDU and re-establishes chemical gradients there. Dotted lines in the figure represent the old results, obtained before our reaction rate updates, while continuous lines represent our new estimates. The vertical dotted line and the dashed one indicate, respectively, the place where  $\Delta = 0.2$  and where the energy from the H-burning shell is maximum ( $T_H$ ). (A color version of this figure is available in the online journal.)

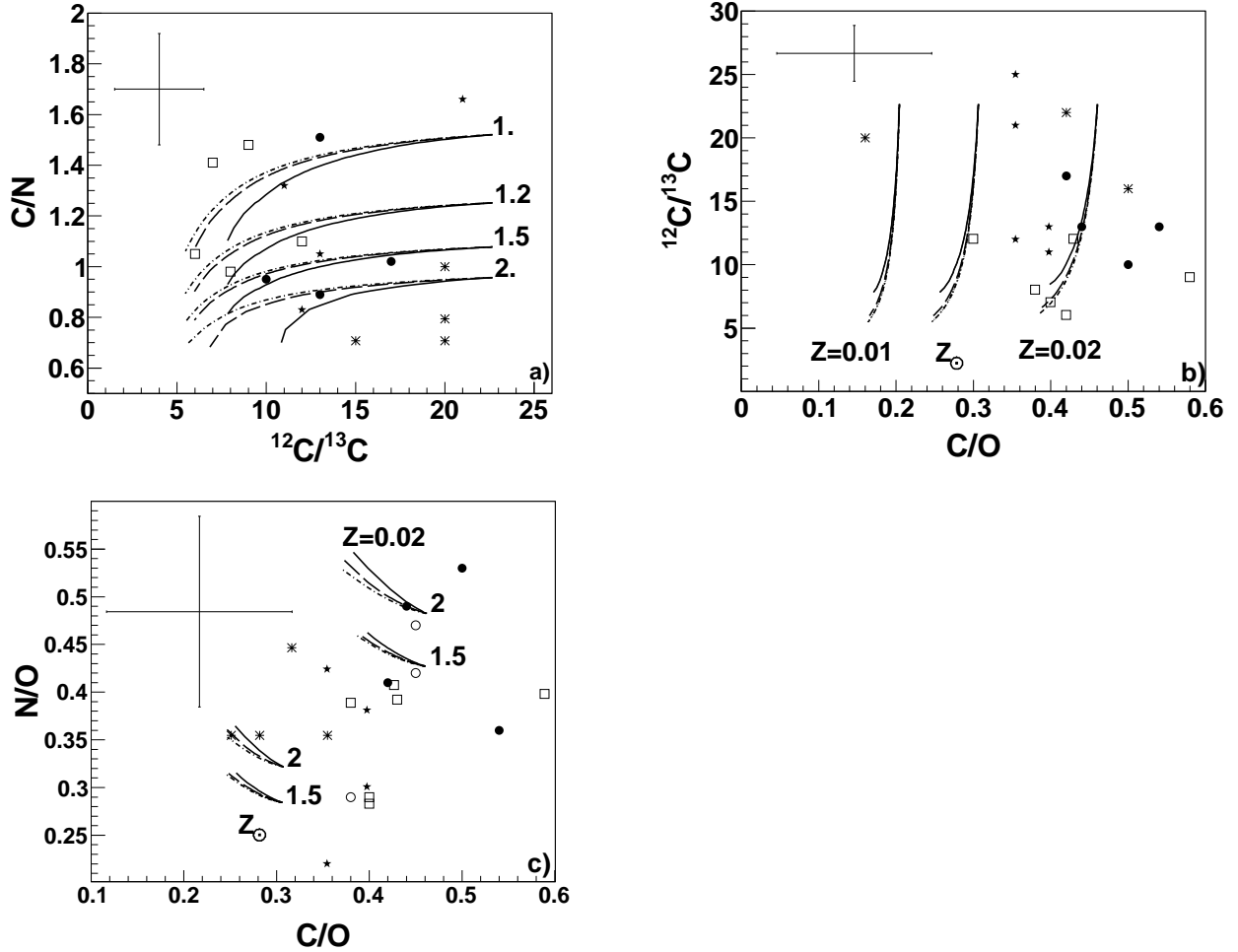


Fig. 5.— Deep-mixing results for CNO nuclei, as compared to observations in RGB stars of metallicities close to solar. Panel a): model curves correspond to  $\Delta = 0.2$ ; they proceed from right to left, starting from abundances at FDU. Continuous lines refer to  $\dot{M}_6 = 0.3$ , dotted lines to  $\dot{M}_6 = 0.1$ , dashed lines to  $\dot{M}_6 = 0.03$ . Black stars show post-FDU stars from M67 (Brown 1987; Gilroy & Brown 1991); asterisks are data from Cottrell & Sneden (1986); open squares refer to open clusters by Mikolaitis et al. (2010). Circles refer to data from Smiljanic et al. (2009), in particular to NGC5822 (filled symbols) and NGC2360 (open symbols). Only solar metallicity models are shown, to avoid excessive crowding; the cases at  $Z = 0.02$  would be slightly shifted upward. The typical uncertainty ( $1\sigma$ ) is indicated. Panel b): same type of comparison, this time for the carbon isotopic ratio versus C/O. Models of  $Z = 0.02$  and  $Z = 0.01$  have been included. Panel c): same comparison, for the N/O versus C/O ratios.

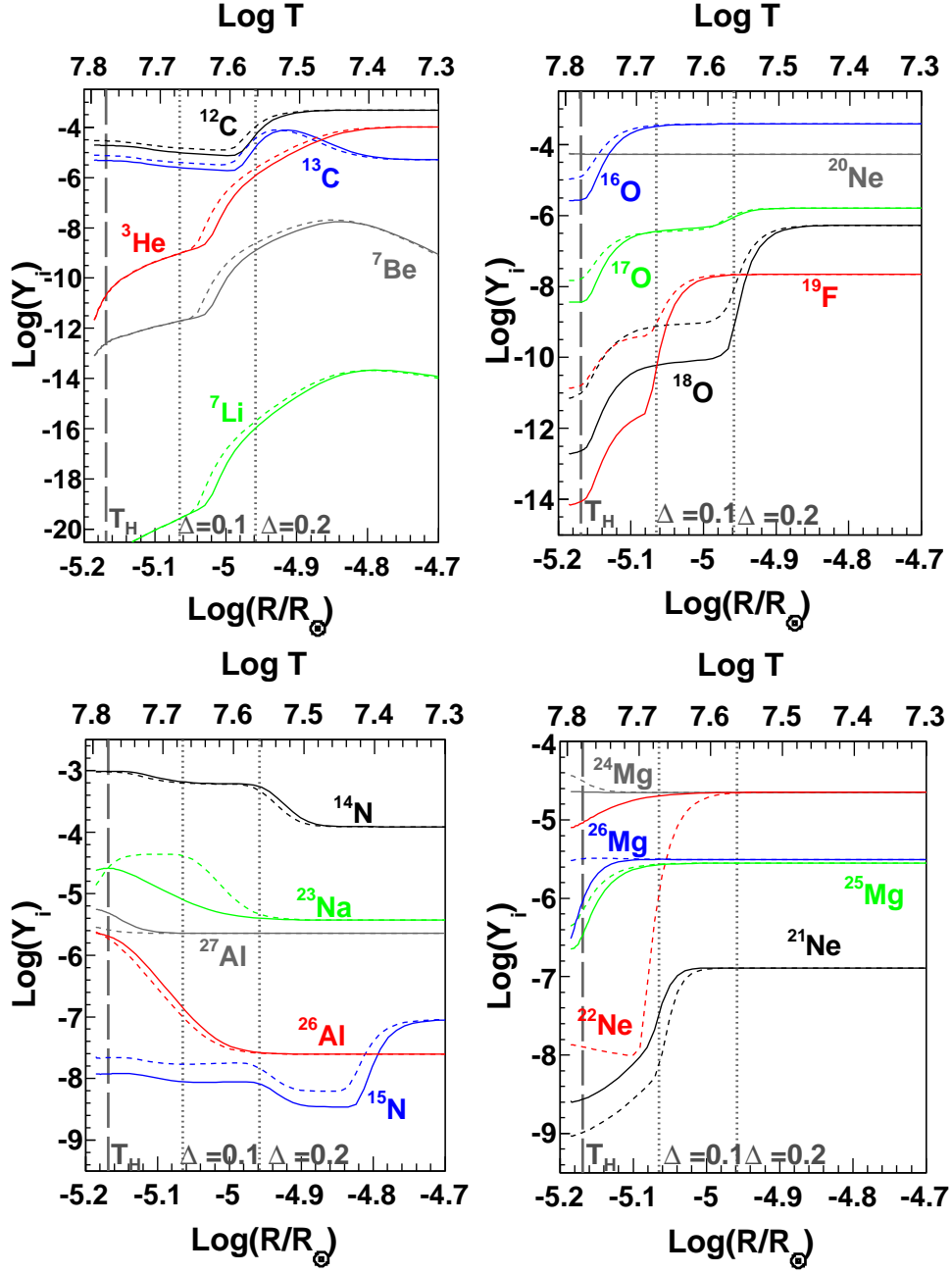


Fig. 6.— Distribution of abundances for some light and intermediate-mass isotopes in the radiative layers between the H-burning shell and the convective envelope. The plots are taken roughly at mid-AGB evolution. The two vertical dotted lines and the dashed one indicate the places where  $\Delta = 0.2$ ,  $0.1$  and  $0.0$ , respectively. This last position corresponds to the layer where the energy from the H-burning shell is maximum (and  $T = T_H$ ). (A color version of this figure is available in the online journal.)

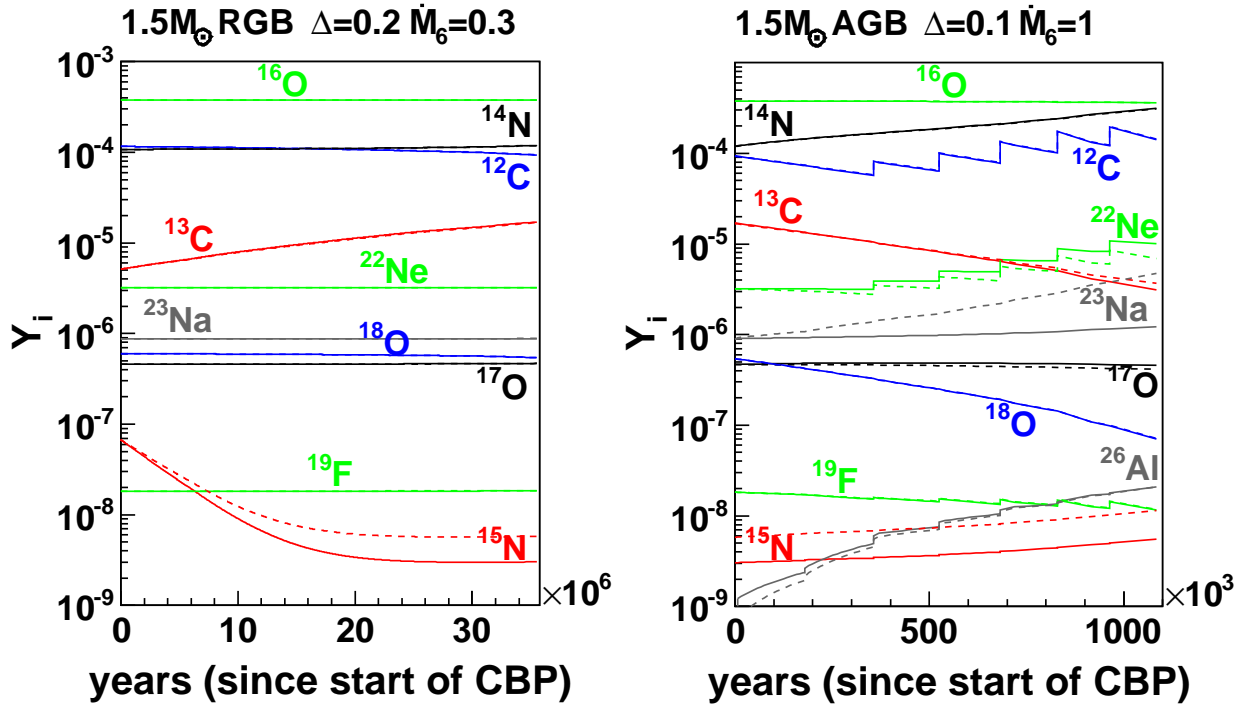


Fig. 7.— An example of the evolution in time of the abundances by mole in the envelope for representative isotopes. The RGB and AGB phases of a  $1.5 M_{\odot}$  star of solar metallicity are shown for a specific choice of the mixing parameters. (A color version of this figure is available in the online journal.)

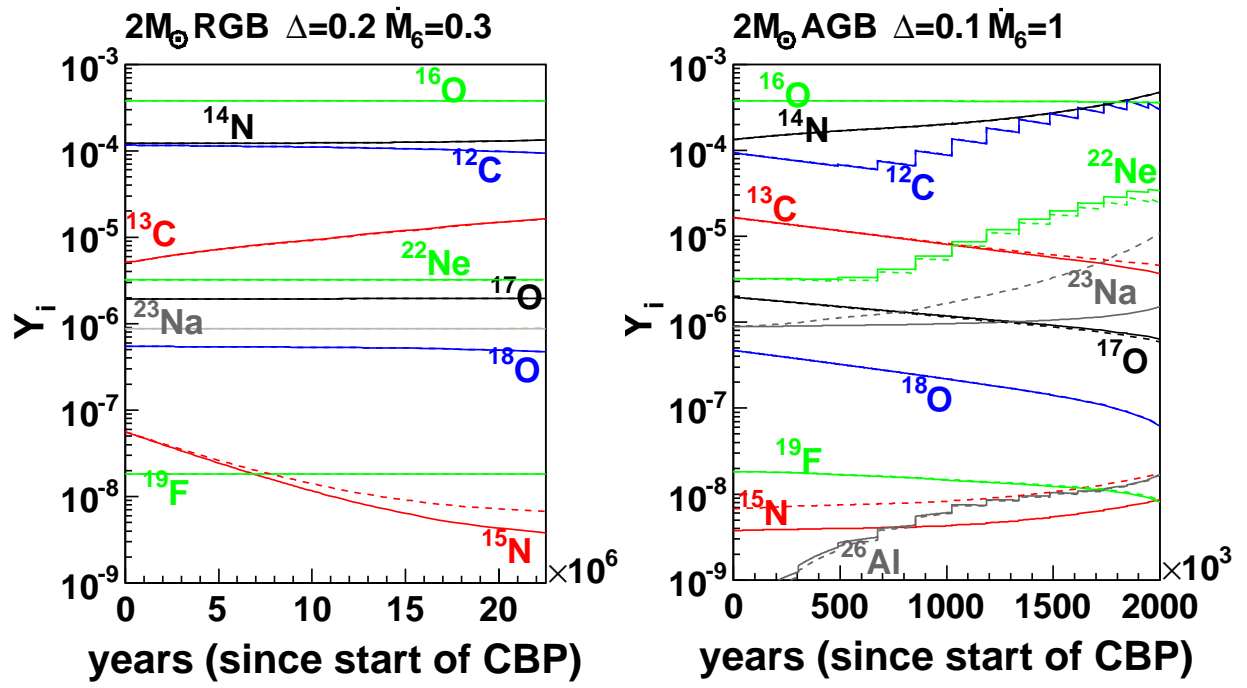


Fig. 8.— Same as in the previous figure, but for a  $2 M_{\odot}$  model star. (A color version of this figure is available in the online journal.)



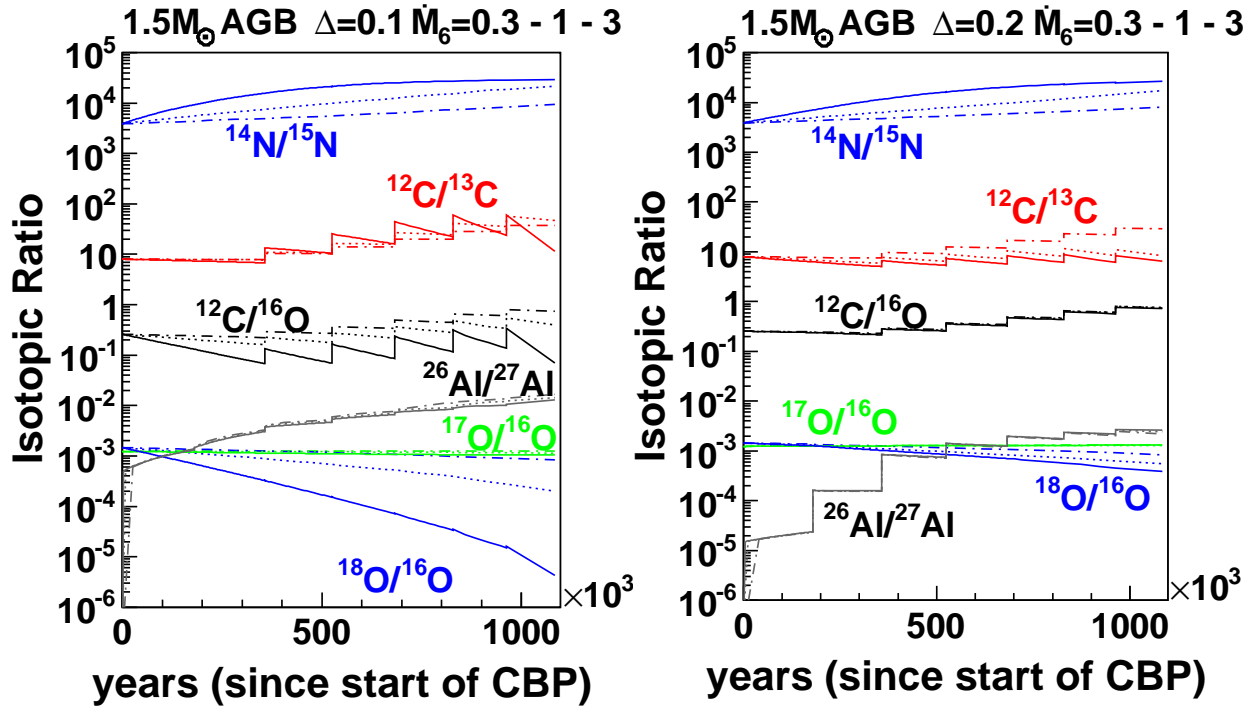


Fig. 9.— Evolution in time of the abundances by mole in the envelope of a 1.5  $M_{\odot}$  star, during the AGB stages. The plot considers three values of the mixing parameter  $\dot{M}_6$  and two choices of the temperature parameter  $\Delta$ . (A color version of this figure is available in the online journal.)

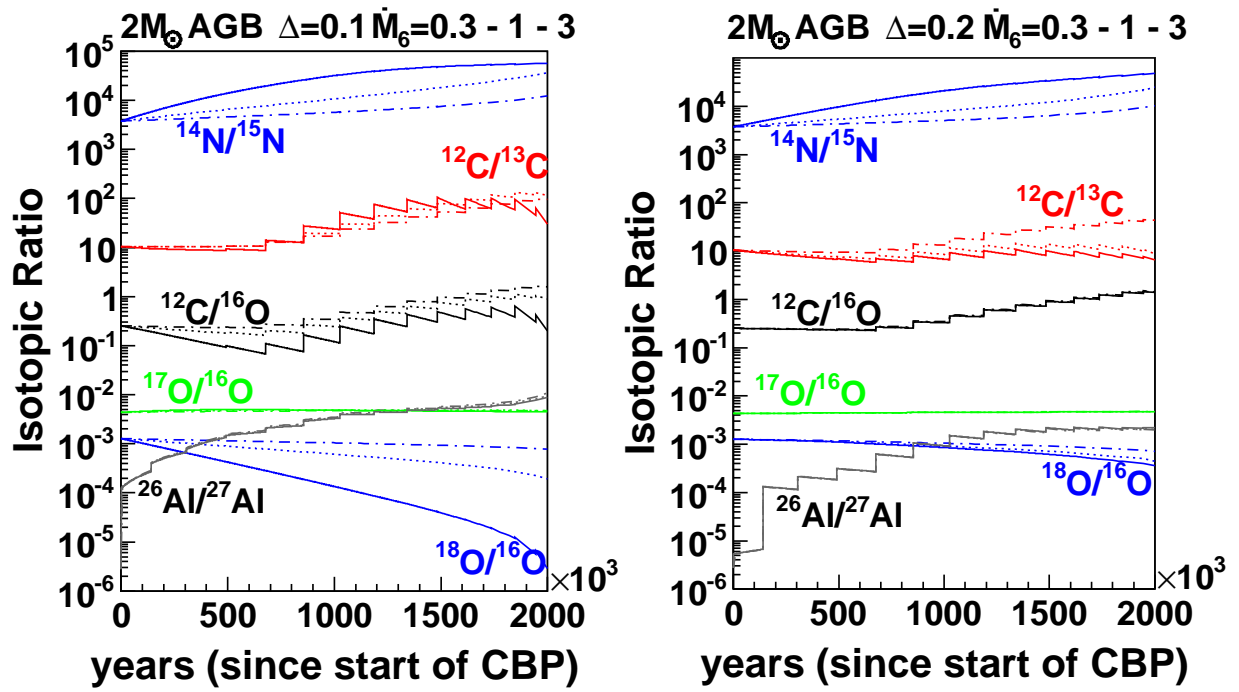


Fig. 10.— Same as in the previous figure, for a stellar model of  $2 M_{\odot}$ . (A color version of this figure is available in the online journal.)

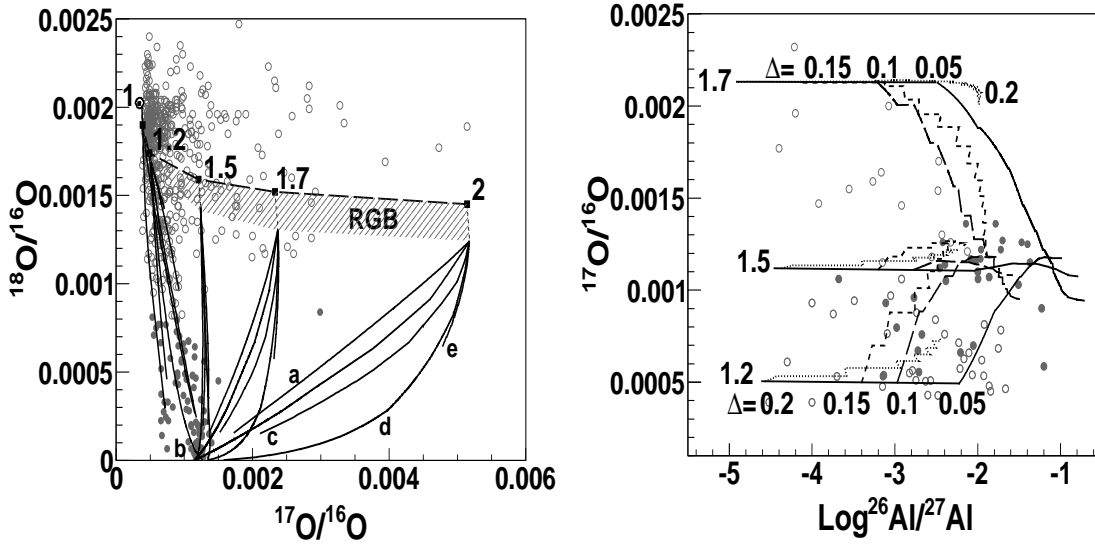


Fig. 11.— The curves show the oxygen and aluminum isotopic mix in the envelopes of our solar-metallicity stars during advanced evolutionary stages, as compared to presolar oxide grain compositions (WUSTL Presolar Database <http://presolar.wustl.edu/pgd/>). Left panel: FDU is indicated by the heavy, long-dashed curve; short-dashed lines and the shaded area show the effects of deep mixing on the RGB, for  $\Delta = 0.2$  and  $\dot{M}_6 = 0.1$ . This is a more moderate choice than in Fig. 3. The symbols for data points are the same as in Fig. 3. Continuous lines refer to model results for extra-mixing on the AGB (all models for a specific mass are named a), b), c), d), e) from left to right). They correspond to specific choices of the parameters, namely: a)  $\Delta = 0.1$ ,  $\dot{M}_6 = 1$ ; b)  $\Delta = 0.1$ ,  $\dot{M}_6 = 3$ ; c)  $\Delta = 0.15$ ,  $\dot{M}_6 = 1$ ; d)  $\Delta = 0.15$ ,  $\dot{M}_6 = 3$ ; e)  $\Delta = 0.2$ ,  $\dot{M}_6 = 1$ . Models for  $M \leq 1.7M_{\odot}$  explain essentially all the data for  $^{18}\text{O}$ -poor grains. In particular, group 2 grains mainly derive from very low-mass stars (below  $1.5 M_{\odot}$ ). Right panel: the  $^{17}\text{O}/^{16}\text{O}$  ratio as a function of the  $^{26}\text{Al}$  content. Continuous lines refer to  $\Delta = 0.05$ ; long-dashed lines to  $\Delta = 0.1$ ; short-dashed lines to  $\Delta = 0.15$ ; dotted lines to  $\Delta = 0.20$ . Model curves proceed from left to right, converging toward the equilibrium  $^{17}\text{O}/^{16}\text{O}$  at the specific temperature of each model. Most of the data points are accounted for (see text for the parameter values).

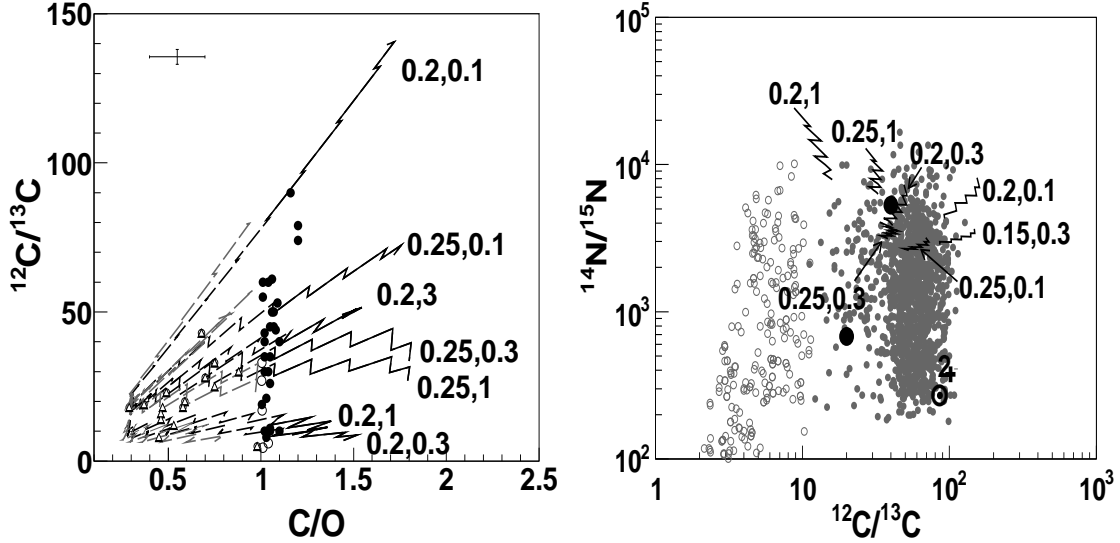


Fig. 12.— Left panel: observations of C/O and  $^{12}\text{C}/^{13}\text{C}$  ratios in AGB stars of types MS, S (white triangles), SC (open circles) and C(N) (filled circles), as compared to a few of our curves from models of 1.5 (grey curves) and 2  $M_{\odot}$  (black curves) at solar metallicity, with extra-mixing and TDU. Continuous lines refer to the C-rich phases, dashed lines to the O-rich ones. The labels indicate the choices for  $\Delta$  and  $\dot{M}_6$ . The area of the data is well covered by the models, indicating that the parameter choices should be rather typical of real AGB stars. Right panel: The  $^{14}\text{N}/^{15}\text{N}$  ratios of SiC grains recovered from pristine meteorites, as a function of their  $^{12}\text{C}/^{13}\text{C}$  ratios. Open symbols represent the A+B grains, grey symbols the so-called "mainstream" ones (Zinner 2005; Zinner et al. 2006, WUSTL Presolar Database <http://presolar.wustl.edu/pgd/>). Model curves are from a 2  $M_{\odot}$  star of solar metallicity; only the final C-rich phases are plotted. Again, the model parameters are indicated. The range of carbon isotopic ratios of mainstream grains and of some A+B grains is reproduced, but our  $^{14}\text{N}/^{15}\text{N}$  ratios are always much larger than solar. The full dots represent stellar measurements by Wannier et al. (1991) in C-rich circumstellar envelopes and confirm that high values are typical of evolved stars. See text for comments. The two symbols 4 and 0 indicate the values of the nitrogen isotopic ratios found in Jupiter, which we use as initial abundance in our models, and in the Sun.

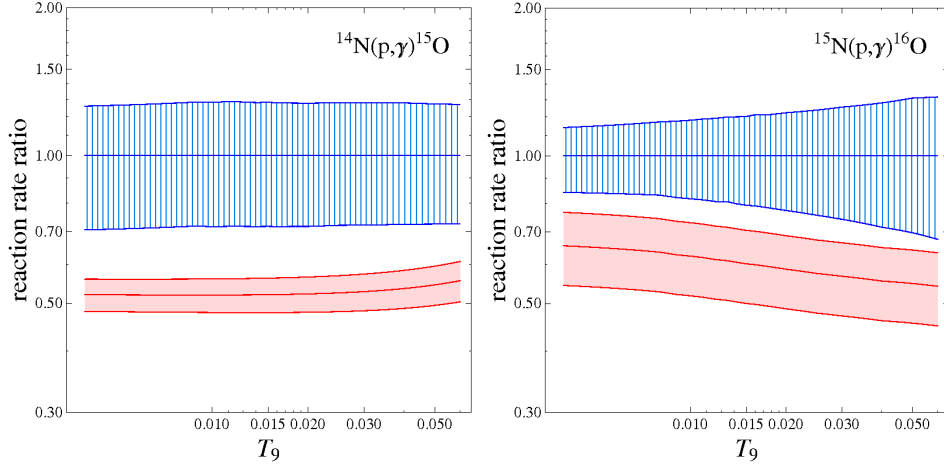


Fig. 13.— Left: a comparison of the NACRE rate for the reaction  $^{14}\text{N}(p,\gamma)^{15}\text{O}$  (hatched blue band) with the updated one from ADE10 (light-red filled band). The solid lines mark the recommended value, together with lower and upper limits (blue for NACRE, red for ADE10). The NACRE rate is adopted as a normalization (i.e. it is taken equal to 1 over the whole temperature region). Right: the same comparison for the reaction  $^{15}\text{N}(p,\gamma)^{16}\text{O}$ . (A color version of this figure is available in the online journal.)

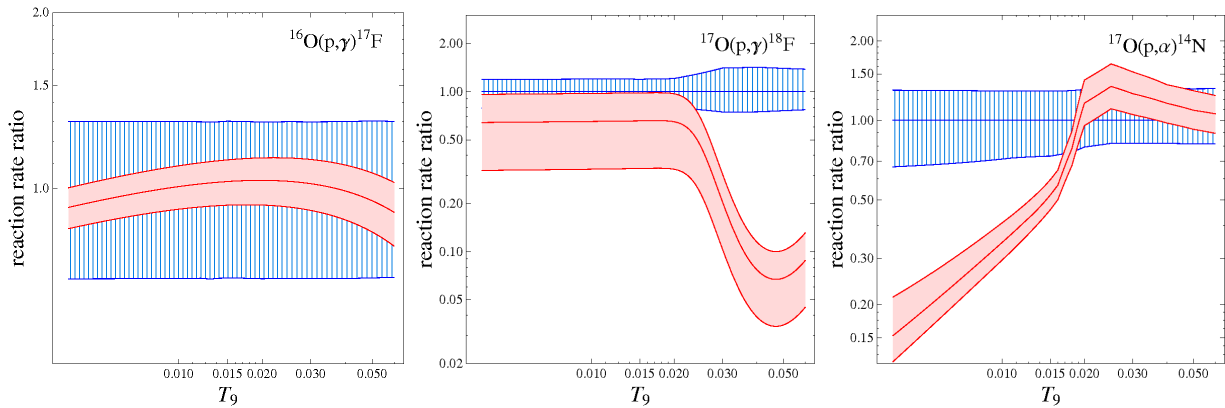


Fig. 14.— Same comparison as in Fig. 13, for the reactions  $^{16}\text{O}(p,\gamma)^{17}\text{F}$ ,  $^{17}\text{O}(p,\gamma)^{18}\text{F}$  and  $^{17}\text{O}(p,\alpha)^{14}\text{N}$ . (A color version of this figure is available in the online journal.)

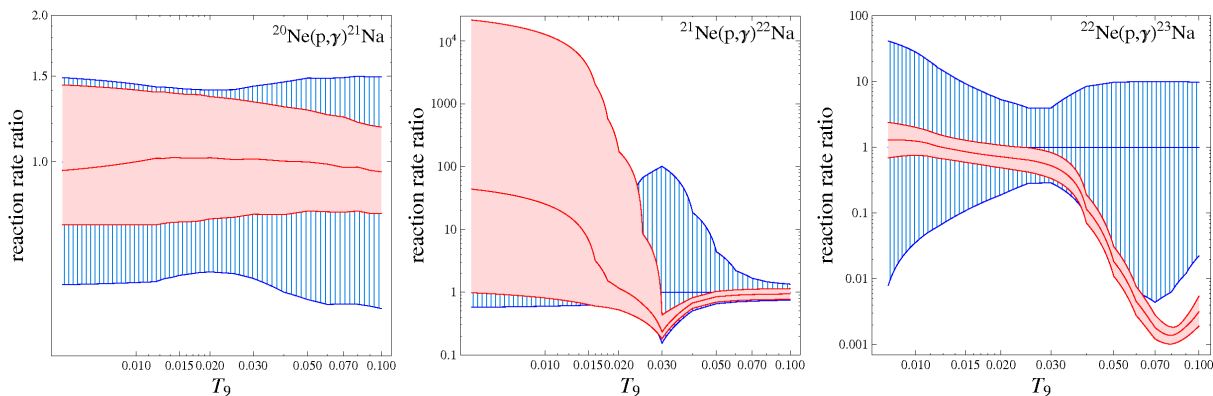


Fig. 15.— Same comparison as in Fig. 13, for the reactions  $^{20}\text{Ne}(p,\gamma)^{21}\text{Na}$ ,  $^{21}\text{Ne}(p,\gamma)^{22}\text{Na}$  and  $^{22}\text{Ne}(p,\alpha)^{23}\text{Na}$ . (A color version of this figure is available in the online journal.)

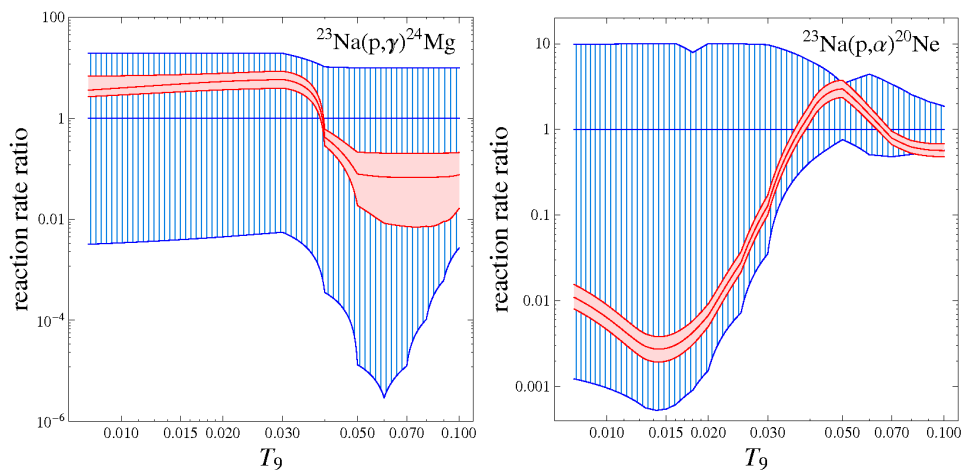


Fig. 16.— Same comparison as in Fig. 13, for the reactions  $^{23}\text{Na}(p,\gamma)^{24}\text{Mg}$  and  $^{23}\text{Na}(p,\alpha)^{20}\text{Ne}$ . (A color version of this figure is available in the online journal.)

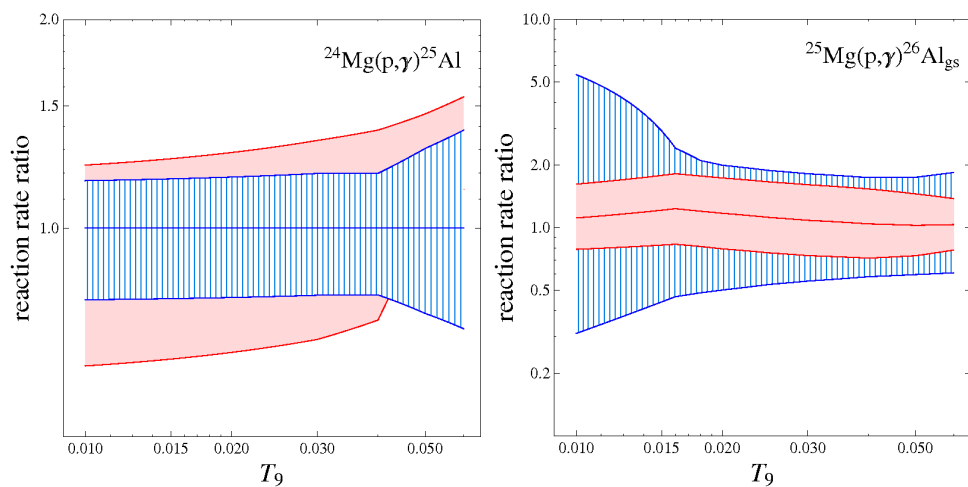


Fig. 17.— Same comparison as in Fig. 13, for the reactions  $^{24}\text{Mg}(p,\gamma)^{25}\text{Al}$ , and  $^{25}\text{Mg}(p,\gamma)^{26}\text{Al}_{gs}$ . (A color version of this figure is available in the online journal.)

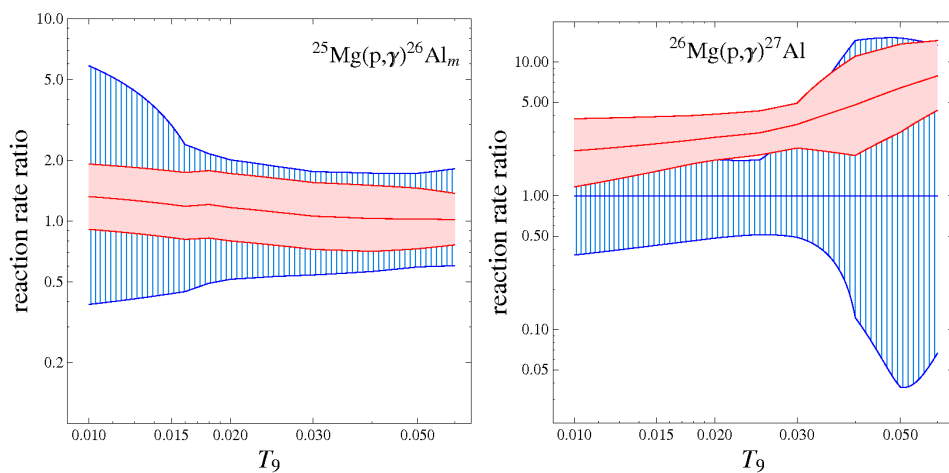


Fig. 18.— Same comparison as in Fig. 13, for the  $^{25}\text{Mg}(p,\gamma)^{26}\text{Al}_m$  and  $^{26}\text{Mg}(p,\gamma)^{27}\text{Al}$  reactions. (A color version of this figure is available in the online journal.)

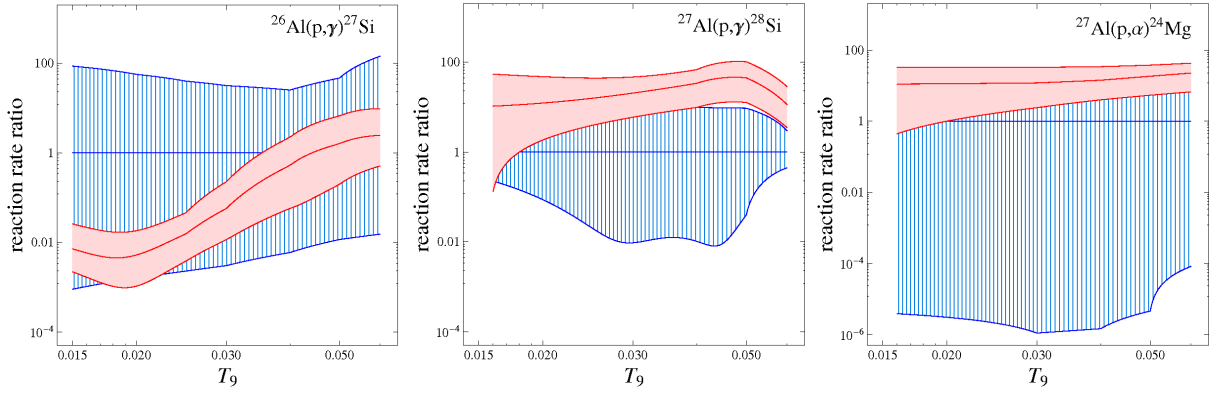


Fig. 19.— Same comparison as in Fig. 13, for the reactions  $^{26}\text{Al}(p,\gamma)^{27}\text{Si}$ ,  $^{27}\text{Al}(p,\gamma)^{28}\text{Si}$  and  $^{27}\text{Al}(p,\alpha)^{24}\text{Mg}$ . (A color version of this figure is available in the online journal.)